Enhancing the Performance of Time-Resolved Spectroscopy

Master's Thesis
by
Erik Alerstam

Lund Reports on Atomic Physics, LRAP-389
Lund, September 2007

Abstract

The work presented in this report can be divided into two parts.

First, a novel scheme for fully scaleable White Monte Carlo (WMC) was developed. This light propagation model was used as a forward model for evaluation of experimental photon migration data from a time-resolved spectroscopic instrument intended for clinical measurements. The use of this model is motivated by the recent interest in the *in vivo* optical properties of organs such as the prostate, where previously used models, e. g. diffusion theory, break down. Both simulations and experimental work on tissue phantoms, were conducted to investigate and compare the performance of diffusion modeling and the proposed WMC model.

Secondly, the performance of the time-resolved spectroscopic instrument itself was reviewed, and an error induced by the measurement of the instrument response function (IRF) was found. An alternative way of measuring the IRF was adapted and were found to resolve the error.

The results of this work should significantly improve the ability to perform accurate spectroscopic analysis of the human prostate *in vivo*.

Sammanfattning

Prostatacancer är den vanligaste formen av cancer hos män i Sverige. Om än många gånger behandlingsbar, så är det en plågsam sjukdom. För att försöka förbättra behandlingsresultaten och göra livet enklare för patienterna håller forskare och doktorer i bland annat Lund på att utveckla nya behandlingmetoder baserade på ljus och ljuskänsliga läkemedel. Dessa behandlingsmetoder bygger i korta drag på att det ljuskänsliga läkemedlet ansamlas i tumören. När läkemedlet belyses med ljus omvandlas det till ett giftigt ämne som effektivt dödar de närliggande cellerna. Om man vet koncentrationen av detta läkemedel kan man därmed styra vilka områden som ska behandlas och vilka som ska skonas genom att belysa olika områden olika mycket. Metoden visar lovande resultat, men har i nuläget två problem: För det första är det inte alltid klart vilka koncentrationer av läkemedlet som faktiskt ansamlas i tumören och för det andra är människokroppen inte genomskinlig på samma sätt som t.ex. ett vanligt fönster. Mänsklig vävnad är genonomskinlig i den mening att ljus inte absorberas i någon större grad, men istället sprids ljus mycket vilket gör att mänsklig vävnad, optiskt sett, är väldigt likt t.ex. mjölk eller grumligt vatten. Detta medför ett problem då det är svårt att få fram tillräckligt mycket ljus för att aktivera läkemedlet om tumören befinner sig innuit kroppen.

Ett led i utvecklingen av ljusbaserade tekniker för behandling av prostatacancer är att lära sig att uppskatta vävnadens optiska egenskaper. Med hjälp av ett så kallat tidsupplöst instrument som kan mäta hur ultrakorta ljuspulser breddas i tiden när de utbreder sig i vävnad. Denna breddning av pulserna beror just på att vävnaden sprider ljuset, vilket gör att ljuset tar en lång omväg när det går igenom vävnaden. Genom att jämföra de breddade pulserna med matematiska modeller för hur ljuset utbreder sig i spridande material, kan man utvärdera de optiska egenskaperna för olika material. Genom att göra detta för olika våglängder (färger) hos ljuset kan man uppskatta koncentrationerna av olika ämnen i materialet och även beräkna hur man på bäst sätt fördelar ljuset i en behandlingssituation.

I detta arbete beskrivs utvecklingen av en ny matematisk model för ljusutbredning i spridande material. Denna model jämförs sedan med tidigare modeller med slutsatsen att den nya modellen borde ge betydligt bättre möjligheter att utvärdera de optiska egenskaperna i material som absorberar ganska mycket ljus, likt prostatavävnad. Det tidsupplösta instrumentet testades också noggrannt, vilket medförde några små men viktiga ändringar i hur instrumentet ska användas.

Den nya modellen och de små skillnaderna i handhavandet av instrumentet visas öka möjligheterna att göra bra mätningar av optiska storheter för prostata och liknande material.

Contents

List of Publications

Paper I
White Monte Carlo for Time-resolved Photon Migration
E. Alerstam, S. Andersson-Engels and T. Svensson
Submitted (2007)

Chapter 1

Introduction

1.1 Background

In the recent years, an effort has been made by the biomedical optics community to utilise photodynamic therapy (PDT) as a modality to treat cancer in humans. PDT is process involving a photosensitizer which accumulates in areas of high metabolism, such as tumours, when introduced in the human body. When the photosensitizer is excited by light it induces cytotoxic oxygen species, oxidizing the nearby tissue and effectively killing it. PDT relies on the presence of oxygen, photosensitizer as well as light. The dosimetry hence proves to be a difficult matter. If the oxygen and photosensitiser concentration in the tumour was known and the light distributions could be accurately modelled and optimised PDT could provide an effective and highly selective way of treating cancer.

The Biomedical optics group in Lund is currently working with a company by the name Spectracure, to develop an instrument to treat prostate cancer using PDT. The optical properties of human prostate is therefor of great interest to the group.

In a recent paper by Svensson *et al.*[1] a Time-Resolved spectroscopic (TRS) instrument was used to investigate the *in vivo* optical properties of human prostate tissue. The advantage of the TRS instrumentation is that it can measure both the scattering properties, μ_s', of the tissue and the light absorption μ_a without using the absolute intensity of the detected light. The information can then be used to do spectroscopy, i.e. calculate the concentration of the major constituents of the tissue. The optical properties, recovered using diffusion theory, are presented in Table 1.1.

Although the study was generally successful the authors encountered some issues that deserved further attention. The major issue was that the scattering did not decrease with increasing wavelength as predicted by general theory on light scattering. An evaluation of the instrument and the mathematical models used to evaluate data was thus initiated. In particular the high μ_a measured in

λ [nm]	μ_a [1/cm]	μ_s' [1/cm]
660	0.5 ± 0.1	8.7 ± 1.9
786	0.4 ± 0.1	7.1 ± 1.6
916	0.6 ± 0.1	7.7 ± 1.8

Table 1.1: The *in vivo* optical properties of human prostate tissue at three different wavelengths, From Reference 1

the prostate suggest that the mathematical model used to evaluate the TRS data may not be valid in this region of optical properties. A more detailed numerical model, based on stochastic simulation of light transport, i.e. Monte Carlo simulations, may be more accurate.

1.2 Goals

Within the overarching goal to improve the performance of the time-resolved system the main objectives of this work were:

- Evaluate robustness, accuracy and reproducibility with respect to photon migration model, measurement geometry, source-detector fibre separation and optical properties of the sample.
- Design, implementation and validation of a Monte Carlo based data evaluation routine to extract the interesting optical properties, μ_s' and μ_a, from experimental data.
- Comparison of Monte Carlo based data evaluation with evaluation based on diffusion theory.
- Support ongoing research on prostate tissue.

1.3 Outline

Chapter 2 will give a brief theoretical background on light transport in turbid media such as tissue. Electromagnetic wave theory is briefly mentioned just to introduce the Transport theory of radiative transfer. Here the optical properties of interest within the field will be introduced followed by a description of two different ways of solving the equations introduced by Transport theory; Analytical solutions based on the Diffusion approximation and numerical solutions based on stochastic Monte Carlo simulations.
Chapter 3 will introduce the instrumentation and the techniques involved in characterisation of turbid media using Time-Resolved techniques.
Chapter 4 will first give a brief introduction to the history of White Monte Carlo and what's been done in the field so far. The rest of Chapter 4 will be a comprehensive explanation of the White Monte Carlo model developed under the

scope of this thesis. Some discussion and results are inevitably included in this chapter as many thoughts, discussions and experiments created the foundation to the work presented here.
Chapter 5 will be an explanation of the Method used for the simulations and measurements performed in this work. Selected results will be presented in Chapter 6 and qualitatively discussed in Chapter 7. More results, providing the link between simulations and experiments, are presented and quantitatively discussed in **Paper I**.
Chapter 8 will briefly state some of the conclusions that can be derived from this work. Chapter 9 will comprise a short list of suggested future work connected to the work presented here.

Chapter 2

Photon Migration Theory

As the theory of light propagation in turbid media previously have been thoroughly covered by many authors this chapter will only give a brief introduction to the field, to make this thesis accessible to people how are not perviously familiar with the subject. The book *Optical-Thermal Response of Laser-Irradiated Tissue* by Welch and van Gemert, Reference 2 provides an excellent and extensive summary of photon migration theory and this book is also the reference for this entire chapter unless otherwise noted. Swartling and Thompson also provide excellent, though much shorter, summaries of the subject and their respective disertation thesises, Reference 3 and 4 respectively, are recommended for the interested reader.

2.1 Introduction

Modelling of light propagation in complex media such as tissue is not an easy task, despite the accurate models developed. The most accurate way of modelling electromagnetic wave propagation, i.e. light, today would be the Maxwell's equations. In this theoretical model, sometimes called Wave theory, the optical properties are described by the complex dielectric constant $\epsilon(\mathbf{r})$ where the real and imaginary parts describe the refractive index (the local speed of light) and absorption properties, respectively. However, most of the information in this model is based on the spatial variations of the dielectric constant and wave theory hence requires an extremely detailed model. This is of course not possible for macroscopic tissue models, but for simple microscopic models, such as small spherical particles of the same size, wave theory can be proved useful. The solution to Maxwell's equations for the former model provides the foundation for Mie scattering theory, which accurately describes how light is scattered when incident on particles roughly the same size as the wavelength of the light.

To model light propagation in a way that can provide usable solutions for macroscopic models of tissue, simplifications have to be made and some physical detail is hence lost. A fairly accurate model is Radiative transport which unfortunately

only provide numerical solutions. Further simplifications and approximations provides Diffusion theory, which provides analytical solutions at the price of reduced accuracy and model constraints. An overview of the mentioned models is shown in Figure 2.1

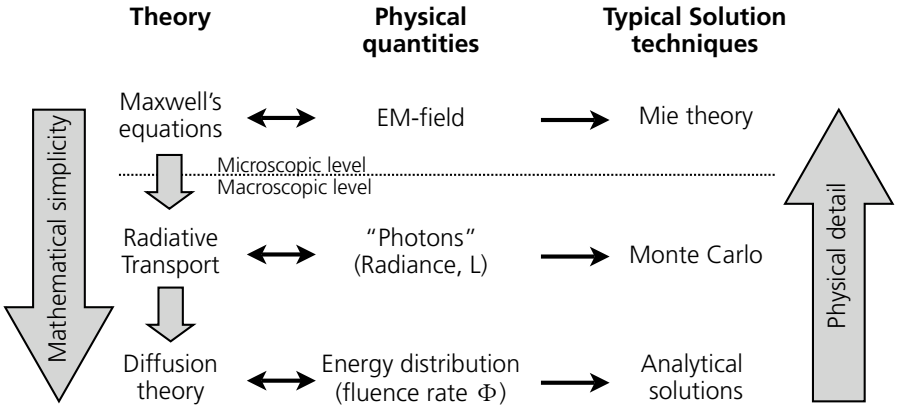

Figure 2.1: Overview of the different approaches to photon migration theory and the respective solution techniques. (Modified from Soto Thompson[4] and Forster[5]).

2.2 Transport theory of radiative transfer

To simplify the light propagation model in turbid media, transport theory is usually preferred. As with all simplifications and approximations some accuracy of the model is lost. In this case all the wave properties of light, for example polarisation and interference, are disregarded. The resulting model describes energy conservation in an infinitesimal small volume as a flux of photons (light particles) passes through and interacts with the medium within the volume element.

The radiative transport equation (RTE) can be written as:

$$\frac{1}{c'}\frac{\partial L(\mathbf{r},\mathbf{s},t)}{\partial t} = -\mathbf{s}\cdot\nabla L(\mathbf{r},\mathbf{s},t) - (\mu_a+\mu_s)L(\mathbf{r},\mathbf{s},t) + \\ +\mu_s\int_{4\pi} L(\mathbf{r},\mathbf{s}',t)p(\mathbf{s},\mathbf{s}')dw' + q(\mathbf{r},\mathbf{s},t), \tag{2.1}$$

where c' is the speed of light in the medium, L is the radiance in the direction $\mathbf{s}$ within the volume element. The first term on the right hand side describes the losses over the boundary of the volume element, the second term describes the losses from absorption and losses from the radiance in a certain direction as light is scattered into other directions. The third term describes the gain from light scattered from any other direction, $\mathbf{s}'$, into the considered direction $\mathbf{s}$. The last term is simply a source term. Despite the simplifications made, RTE proves to be hard to solve without further simplifications, such as discretization of the directions considered or the diffusion approximation. However, RTE introduces

the concept of discrete scatterers and absorbers as opposed to the continuous variations of the permeability used by wave theory. This makes it possible to describe the scattering and absorption properties of a medium using only three parameters, μ_s, μ_a and a phase scattering function, p.

2.2.1 Scattering phase function

The scattering phase function is a function that describes how a lightwave propagate after striking a scatterer. In wave theory the scattering phase function would consist of several lobes as the wave would interfere with itself as it was scattered. The position of the lobes would be dependent on the wavelength of the wave and the size and shape of the scattering particle. In RTE the scattering phase is an average of scattering against particles of different sizes and the lobes are hence averaged out, providing a smooth angular probability distribution describing the probability of scattering in different directions. In the case of perfectly spherical scatterers of the same size Mie-theory would provide an almost perfect scattering phase function but this is rarely the case in tissue. Instead the Biomedical optics community has adapted a scattering phase function from the field of astrophysics called the Henyey-Greenstein function:[6]

$$p(\cos\theta) \equiv \frac{(1-g^2)}{2\left(1+g^2-2g\cos\theta\right)^{3/2}}, \tag{2.2}$$

where g is is the so called the scattering anisotropy factor or g-factor. The definition implies that g is equal to the average of the cosine of the scattering angle, $g = \langle\cos\theta\rangle$. The g-factor is hence a number between -1 and 1, describing the anisotropy. $g = -1$ means all light will be back scattered, $g = 1$ means all light will be forward scattered and isotropic scattering (for which the scattering in all angles are equal) is characterized with a g-factor equal to zero. Figure 2.2 illustrates this. The g-factor is usually in the range of 0.7-1 for tissue and tissue phantoms.

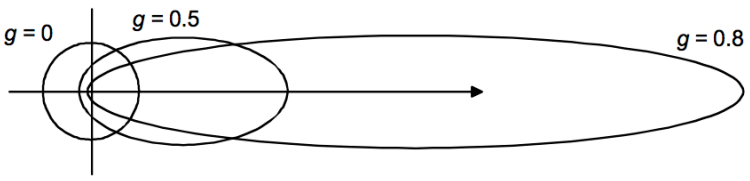

Figure 2.2: An illustration of the Henyey-Greenstein phase function for three different values of g. Adapted from Swartling.[3]

2.2.2 Scattering

Scattering occurs when light interacts with structures, roughly the same size as the wavelength of the light, featuring a change in refractive index. In the case of tissue these structures are for example cells, cell organelles and lipids.

Discretizing this concept on a macroscopic scale gives a coefficient, μ_s, describing the probability of scattering per unit length.
As the size of the structure relative to the wavelength of the light is of importance it is not hard to imagine that the scattering power of a medium will depend on the wavelength of the light. The relationship between the scattering coefficient and the light wavelength is given by Eqn. 2.3:

$$\mu_s = A \cdot \lambda^{-b}, \tag{2.3}$$

where A and b are constants and b is roughly $2 - 3$ for the Mie-like scattering of tissue.

In many case it is convenient to express the scattering in another way, as a reduced scattering coefficient, μ_s':

$$\mu_s' = \mu_s(1 - g). \tag{2.4}$$

The relevance of this quantity is that as the photon is scattered many times it looses track of it's initial direction and it will be hard to separate μ_s and the g-factor in a measurement situation. Instead the phase scattering is assumed to be isotropic and the scattering probability is described by μ_s' rather than μ_s. Over long distances this implies that a high μ_s and low g provides the same light distribution as a low μ_s and high g as long as μ_s' is the same.

2.2.3 Absorption

As a photon encounters a molecule with an electronic transition or rotational-vibrational state matching the energy of the photon there is a chance that the photon will be absorbed, transferring the energy to an excited state of the molecule. As a match between the photon energy and the absorpers energy levels is crucial for an absorption event to occur, the absorption depends strongly on the wavelength of the light.
The probability of absorption per unit length is described by the absorption coefficient for the substance, μ_a, which is actually the product of the extinction coefficient, ϵ [$\mathrm{M}^{-1}\mathrm{m}^{-1}$], and the concentration of the absorber, c [M]. As tissue usually is made up off several constituents, each with a different absorption spectra, the total absorption coefficient can be written as:

$$\mu_a(\lambda) = \sum_k \epsilon_k(\lambda) c_k. \tag{2.5}$$

The absorption spectra of the main absorbers in tissue can be seen in Figure 2.4. By looking at this figure it is clear that there is a region, 650 to 1300 nm, where the overall absorption is fairly low and where the penetration depth of light would be greatest. This region is sometimes referred to as the "Tissue Optical Window".

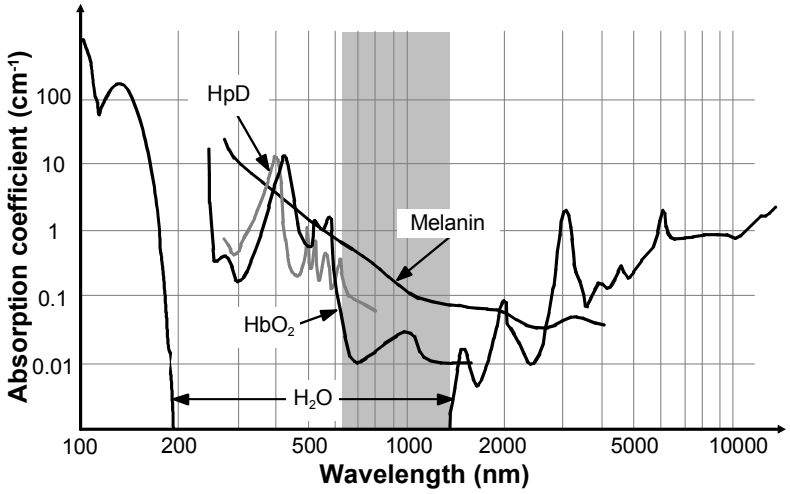

Figure 2.3: The absorption coefficients of some of the constituents of tissue. The Tissue optical window, where the absorption is low, is marked in grey. From Reference 4

2.3 Modelling light distribution in tissue

To actually model light distribution in any turbid media one has to find solutions to the theory describing light propagation. As illustrated by Figure 2.1 the RTE can be solved by numerical solvers, such as Monte Carlo simulations, but if analytical solutions are sought, further simplifications have to be made Even though several solution techniques exists the only one covered here, and perhaps the most utilised, is Diffusion theory, as it is the standard technique to evaluate time resolved data today. A thorough derivation of the analytical solutions to the Diffusion equation is provided by Star in Reference 7 and this is also the source of information for Section 2.3.1 unless otherwise noted.

2.3.1 Diffusion Theory

Diffusion Theory is a way of reducing the RTE to a mathematically simple diffusion equation, commonly encountered in many other areas of physics such as heat transfer. This is done by expanding the radiance L of the RTE into spherical harmonics:

$$L(\mathbf{r},\mathbf{s},t) = \sum_{l=0}^{\infty}\sum_{m=-l}^{l}\sqrt{\frac{2l+1}{4\pi}}L_{lm}(\mathbf{r},t)Y_{lm}(\mathbf{s}). \tag{2.6}$$

The source term is expanded in the same way and the $N+1$ higher order terms of the two expansions are truncated, called the P_N-approximation. By further assuming an isotropic light source, Q, and and inserting the truncated

expansions in the RTE yields the time dependent diffusion equation:

$$\frac{1}{c'}\frac{\partial\phi(\mathbf{r},t)}{\partial t} = \nabla\left(D\nabla\phi(\mathbf{r},t)\right) - \mu_a\phi(\mathbf{r},t) + Q(\mathbf{r},t), \tag{2.7}$$

where ϕ is the fluence rate we are interested in and D is the diffusion constant. The definition of D has been a matter of debate lately, but will in this work be defined in the absorption independent way:[8]

$$D = \frac{1}{3\mu_s'}. \tag{2.8}$$

Solution for infinite homogenous media

Solving Eqn. 2.7 for an infinite homogenous medium and an infinitely short light pulse gives:[9]

$$\phi(r,t) = c'E_0(4\pi c'Dt)^{-3/2}\exp\left(-\frac{r^2}{4c'Dt}\right)\exp(-\mu_a c't), \tag{2.9}$$

where E_0 is the pulse energy and r is the distance from the pulse source. An interesting thing to note is that the second exp() term simply is Beer-Lamberts law.

Solution for semi-infinite homogenous media

Analytical solutions are also available for semi-infinite homogenous media. Since this clearly is hard to describe using spherical symmetric functions the main idea has instead been to place negative sources at opposite side of the boundary or an imaginary boundary to replicate different boundary conditions. The cost of this simplicity is once again lost accuracy. An excellent review of different solutions for the semi-infinite case and comparison to Monte Carlo simulations is available in Reference 10.

Sources of error

Looking back at the approximations and assumptions made to get to Eqn. 2.9, there are two important things to remember: Using an expansion into spherical harmonics is usually a good approximation in case of spherically symmetrical problems. To transform the non-isotropic scattering to a isotropic scattering case it was assumed that the photons can scatter several times without being interrupted, i.e. absorbed.[4] Hence it is assumed that:

$$\mu_a << \mu_s'$$

Also, since the light source usually is directional, statistically the light has clearly not lost its directinalioty until $1/\mu_s'$ from the source. A directional source is therefore usually approximated with an isotropic source located $1/\mu_s'$ from the directional source. This implies that diffusion will be an increasingly bad approximation the closer to the source.[4]

2.3.2 Monte Carlo

The Monte Carlo method is a numerical solution to the RTE suitable for complex geometries that diffusion theory cannot handle. The method is based on tracing photon "packet" trajectories in a random walk through the considered model. This is done by adapting the discrete scatterers and absorbers way of thinking, as supposed by transport theory, where μ_s and μ_a are considered probabilities of interaction per unit length travelled. The theory presented here is based on work by Prahl *et al.*[11] and Wang *et al.*[12] as this is the de facto standard for Monte Carlo simulations within the field of Biomedical Optics today through the open source program MCML.[12]

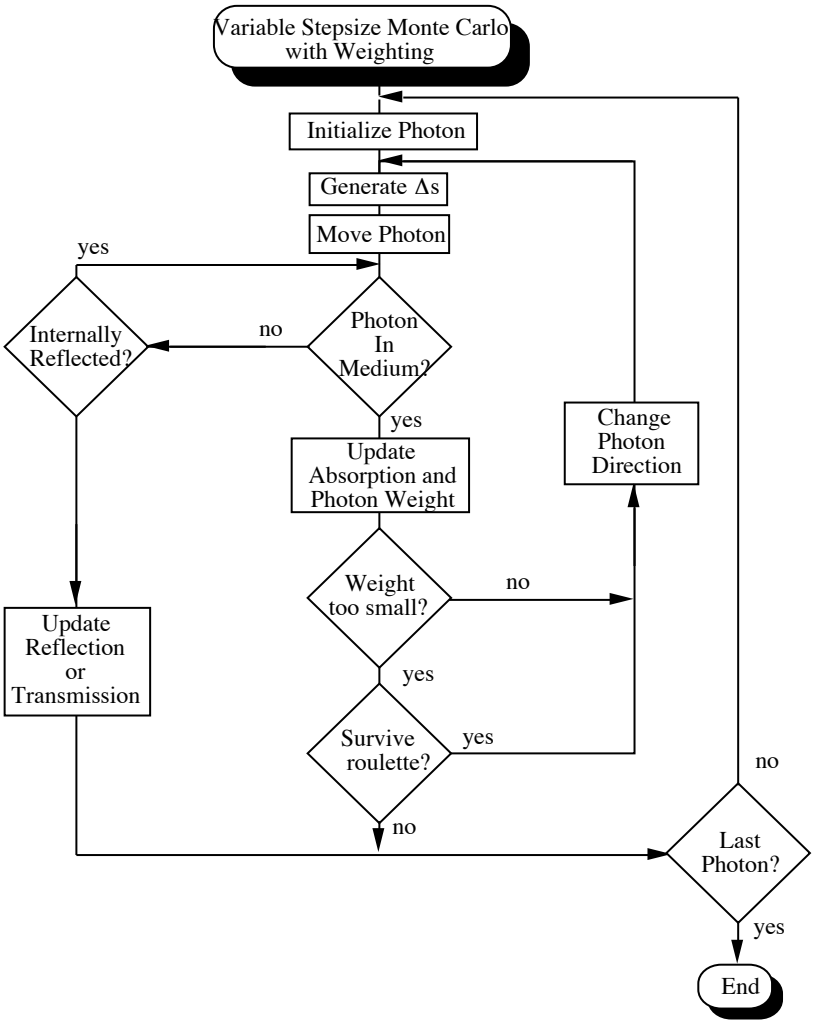

Figure 2.4: A flowchart of traditional Monte Carlo with variable stepsize. From Reference 11.

Packet Initialisation

First the photon packet is initialised, i.e. it is launched into the medium. This includes setting the position, direction and resetting the weight of the photon packet. Often the position is set to origo of the coordinate system and the direction along one of the axis of said coordinate system, simulating an infinitely thin pencil beam.

Moving the packet

The step size Δs is randomised according to an exponential attenuation model, similar to Beer-Lamberts Law, to describe how far the packet will travel before it interacts with tissue by either absorption or scattering. In practice this is done by sampling a random, or in most cases a pseudo random variable, ξ, in half-open[13] interval (0,1] ($0 < \xi \leq 1$) and calculating Δs:

$$\Delta s = \frac{-\ln(\xi)}{\mu_t}, \tag{2.10}$$

where $\mu_t = \mu_s + \mu_a$ is the total attenuation coefficient.

The packet is now simply moved the distance Δs along it's current direction.

Reflection

In case the generated stepsize and photon direction indicates that the photon will cross the boundary to another medium featuring a different index of refraction reflection and refraction has to be accounted for.

This is done by calculating the probabilities of Fresnel reflection determined by the Fresnel reflection coefficient $R(\theta_i)$:

$$R(\theta_i) = \frac{1}{2}\left(\frac{\sin^2(\theta_i - \theta_t)}{\sin^2(\theta_i + \theta_t)} + \frac{\tan^2(\theta_i - \theta_t)}{\tan^2(\theta_i + \theta_t)}\right), \tag{2.11}$$

where θ_i and θ_t are the angles of incidence and transmission respectively, the former calculated by:

$$n_i \sin\theta_i = n_t \sin\theta_t. \tag{2.12}$$

The reflection coeffiecient, $R(\theta_i)$, is then simply compared to a random number ξ sampled in the closed interval [0,1]. $\xi \leq R(\theta_i)$ indicates reflection and $\xi > R(\theta_i)$ indicated transmission and refraction.

Absorption

After each step, the weight of the package is reduced slightly based on the relation between the absorption coefficient and the total attenuation coefficient:

$$fraction\ absorbed = \frac{\mu_a}{\mu_t} = 1 - \frac{\mu_s}{\mu_t} = 1 - a, \tag{2.13}$$

where a is the albedo. Hence the new weight, w', is the product of the old weight, w and the albedo a:

$$w' = aw \tag{2.14}$$

In case the 3D photon distribution is sought after the lost weight, $w_{lost} = (1-a)w$, is stored in the volumetric element defined by the detection grid as illustrated in Figure 2.5

Packet Termination

After the weight of the packet has been reduced a quick check is made to see if the weight of the packet is sufficiently large for the simulation to continue. However, packet that don't clear the check cannot simply be terminated, since that would violate the energy conservation that the Radiative transfer theory is built upon. Instead a technique called "Roulette" is utilised to statistically ensure energy conservation. This is done by, for example, terminating 9/10 packets and instead increasing the weight of the remaining 1/10 packets by a factor 10.

Scattering

After all the weight related calculations are done the packet is scattered, i.e. a new direction is calculated. In case of anisotropic scattering the deflection angle, θ is sampled using the Henyey-Greenstein function, Eqn. 2.2. This is done by sampling a random variable, ξ, in the closed interval [0,1] and calculating θ using:

$$\cos\theta = \frac{1}{2g}\left(1 + g^2 - \left(\frac{1-g^2}{1-g-2g\xi}\right)^2\right). \tag{2.15}$$

The azimuthal angle, ϕ, is selected by sampling a random variable in the interval [0,1) and multiplying by 2π:

$$\phi = 2\pi\xi. \tag{2.16}$$

The new packet direction is calculated from the old direction and the above pair of angles.

Photon Detection

How the photon distribution is recorded depends on the geometry and the nature of the sought distribution. In many cases, such as simple layered structures or homogenously scattering media, the distribution will be cylindrically symmetric. In this case a simple $r-z$ grid with spatial resolution dr and dz can be used to keep track of the photon weights deposited in each volume element if the spatial energy distribution is of interest. If diffuse reflectance is the only

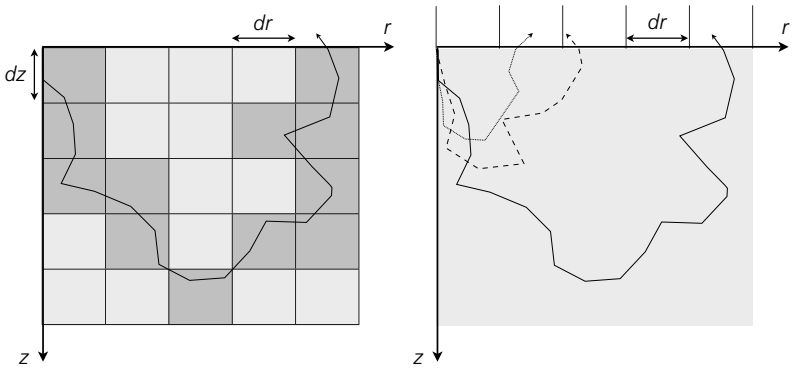

Figure 2.5: An illustration of photon packet detection in most existing Monte Carlo implementations. *Left*: A detection grid with spatial resolution dr and dz in a cylindrical geometry. Each time a photon scatters inside a grid element, the absorbed weight is added to the total absorbed dose of that element. All the elements where the featured photon packet deposits weight are marked by a darker shade of grey. *Right*: A semi-infinite cylindrical geometry where the diffuse reflectance is recorded with spatial resolution dr. In this case the three features photon packets add their respective weight to element 2, 3 and 5 as they leave the medium.

thing considered, a simple radial vector can be used to keep track of the radial distributions of photons leaving the medium. Both of these cases are illustrated in Figure 2.5.

Time Resolution

Even though no de facto standard program exists to keep track of temporal variations in the photon distributions it is very easy to implement, in any existing Monte Carlo code, such as MCML [**?**, wang95]

The local speed of light within the medium, c' is simply the speed of light divided by the refractive index of the medium, $c' = c/n$. Hence, for a step, Δs, the elapsed time for this step is:

$$\Delta t = \frac{\Delta s}{c'}. \tag{2.17}$$

An important aspect of time-resolved Monte Carlo is the increased complexity in detection since an extra dimension has to be recorded. This means that the total number of detection bins will be multiplied by the number of temporal bins requested. Also more photons will most likely have to be simulated to get decent statistics in all temporal channels.

Chapter 3

Time-Resolved Photon Migration Instrumentation

Instruments built to measure Time-resolved photon migrations are a class of instruments were short (picosecond) light pulses are sent into the turbid medium of interest. As the pulses propagate through the medium, they are broadened in time and this broadening is recorded by the instrument. The advantage of this is that absolute light intensity measurements are not required. By comparing the shape of the broadened pulse to models of light transport, information of both the scattering and absorption of the medium can be extracted from a single measurement.

Measuring temporal variations in the order of picoseconds (10^{-12} s) is not an easy task as most detectors simply don't have the bandwidth to resolve such fast variations. Within the field of biomedical optics two different techniques have been adapted from other fields of science to solve this problem, streak camera systems and a technique called Time Correlated Single Photon Counting (TCSPC). The experimental work done within this work was done using a TCSPC system and from hereon this will be the only system considered.

Becker provides a profound perspective on everything related to modern TCSPC techniques in Reference 14. As the following section is a very brief review of TCSPC, the interested reader is referred to Becker's book for more information. Classic papers on Time-resolved measurements of optical properties within the field of biomedical optics are available by Patterson *et al.*[9] and Jacques,[15] among others.

3.1 TCSPC

TCSPC is a technique adopted for the field of physical chemistry where for example very short fluorescence lifetimes are of interest. As the name implies the technique relies on the ability to count single photons and hence require very

little light actually reaching the detector. This makes the technique ideal for applications within the field of biomedical optics as the photon migration models often are increasingly accurate with increased source-detector separation while input power must be minimised and the sample often feature high attenuation.

The TCSPC technique works by sending a very short light pulses into the sample at high repetition rate. By making sure that the probability of a photon reaching the detector in each period is far less than one, a non-biased measurement is ensured, since two photons reaching the detector in the same period would result in only the first photon being detected. The transit time for each detected photon is recorded and a histogram of the recorded photon transit times is constructed. A high repetition rate ensures a fast histogram build up and the histogram is a very exact recording of the optical waveform in the time domain, i.e. a recording of the temporal broadening of a short light pulse by the system (sample and instrument).

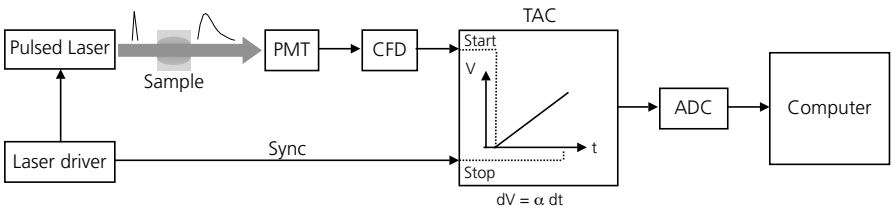

Figure 3.1: A schematic illustration of a typical TCSPC system used for time resolved spectroscopy.

Figure 3.1 shows a schematic picture of a typical TCSPC system. A high repetition rate laser driver sends a train of pulses to a laser. The short light pulses generated by the laser are guided into the sample by the means of for example fibre optics. Another optical fibre collects light and guides this to the detector. The detector has to be very sensitive since it has to be able to detect single photons. Detectors that manages this are for example cooled photo multiplier tubes (PMT) and sensitive avalanche photodiodes. Due to the amplification jitter of sensitive detectors, such as PMT's, the signals for the detector is sent to a constant fraction discriminator (CFD). The CFD triggers at a constant fraction of the pulse amplitude to avoid timing jitter due to the fluctuating amplitude of the signal. The CFD also excludes pulses that are below or above certain thresholds, thus reducing noise. The signal from the CFD is sent to a time to amplitude converter (TAC). The TAC is a component that measures the time between two electrical pulses and converts this time into a voltage. The intuitive way of using the TAC would be to start the TAC using the Sync signal from the laser driver and use the signal from the detector, via the CFD, to stop. This would, however, limit the repetition rate of the system to the repetition rate of the TAC, which is fairly slow as the TAC basically is a capacitor that has to be charged/uncharged every period. Instead most TCSPC systems use a so called Reversed Start-Stop mode where the detector signal is used to start and the Sync is used to stop the TAC. This makes it possible to run the system at much higher repetition rates as photons rarely reach the detector. As long as far less photons reach the detector per second than the maximum repetition

rate of the TAC this works fine and can increase the overall maximum photon count rate of the system. The resulting pulses form the TAC are sent to a fast analog to digital converter (ADC) connected to a computer which bins the pulses according to voltage into sought after histogram.

3.2 Instrument Response Function

The recorded histogram does not, however, describe just the transfer function (temporal broadening of an impulse) of the sample but also includes the temporal broadening induced by the instrument itself. The total temporal broadening of the instrument, called the instrument response function (IRF), describes the convolution of the impulse response of all the individual components in the system. This includes the pulse shape from the light source, the dispersion in the fibre optics and the pulse broadening by the detector, cables and all the electronics.

To retrieve the function describing the impulse response of the sample, the measured histogram must be de-convoluted with the IRF, which of course has to be measured. How the IRF is measured depends on the system, but it is usually a matter of measuring without a sample in place. It is evident that the IRF is a major factor limiting the resolution of a TCSPC system and great care has to be take to measure the true IRF of the system as an erroneous IRF will affect the results.

Another aspect of the IRF is that it is used to keep track of temporal drifts in the system. As picosecond resolution is required several effects such as temperature dependent delay in cables and temporal drifts of the light source becomes of importance. By recording the IRF just before and after or even in parallel with the intended measurements, such drifts can be monitored and accounted for. Ideally the IRF would be recorded simultaneously with the measurements to be able to account for fast temporal drifts, but this is hard to achieve as the IRF should be measured with the same fibres as the measurements are performed with. A possible solution would be to guide a small portion if the light going into the source fibre, via an optical fibre to the detector to provide a temporal reference for each measurement. The IRF could then be shifted with respect to this reference to handle the drifts. Yet another way to handle drifts would be to insulate and temperature stabilise the entire system, as temporal drifts account for the major part of the drifts even after the system has warmed up.

3.3 Data analysis

The strength of the time-domain instruments within the field of biomedical optics is their ability to extract information on both the scattering and absorption of the sample from a single measurement compared to spatially resolved instrument which only provides information on the effective attenuation, $\mu_{eff} = \sqrt{3\mu_a(\mu_a + \mu'_s)}$. This is done by comparing a theoretical model of time-

resolved light propagation to the experimental data. As most theoretical models usually describes transfer function of a sample and de-convolution of the experimental data might provide a noisy result, the currently most utilised way is to convolute the theoretical model with the measured IRF and then compare it to the experimental model. Denoting the theoretical model (as a function of μ_s' and μ_a), convoluted with the IRF, $v_i(\mu_s', \mu_a)$ and the experimental data y_i, where i is the channel number, the problem can be written as minimization problem of the merit function:

$$\chi^2(\mu_s', \mu_a, k) = \sum_{i=1}^{N} \left(\frac{y_i - k \cdot v_i(\mu_s', \mu_a)}{\sigma_i} \right)^2, \tag{3.1}$$

where N is the number of channels involved, k is a free amplitude parameter and σ_i are the weights of trustworthiness of the individual channels. This is a case of non-linear curve fitting which usually is solved by a non-linear optimisation algorithm such as the Levenberg-Marquardt algorithm.[16,17]

A non-linear optimization algorithm, evaluating experimental time-resolved data is schematically illustrated in figure 3.2. This is called a forward solver since it utilizes a forward model, generating a temporal dispersion curve from a set of parameters, even though the opposite is requested.

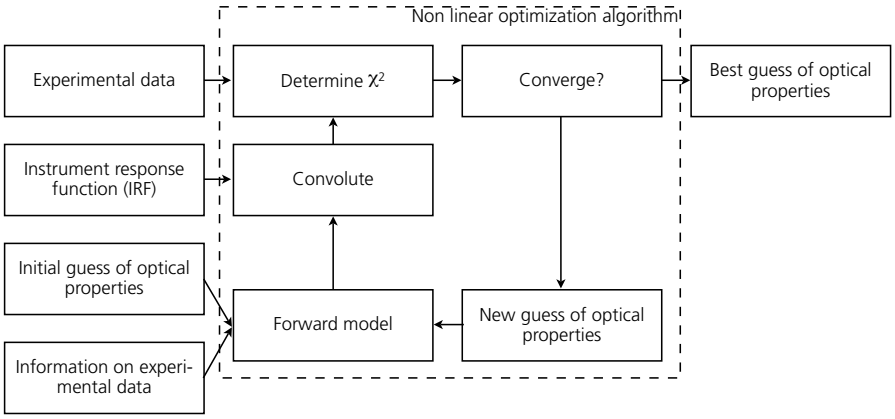

Figure 3.2: A schematic illustration of a non-linear optimization algorithm, using a forward model to evaluate the optical properties from experimental data. The forward model can be any model, Diffusion, Monte Carlo or any other as long as it's fast enough for the solver to converge in reasonable time.

3.4 Spectroscopy

An interesting possibility using the TCSPC system is that it is possible to use several light sources and hence extracting the optical properties of a sample simultaneously from a single measurement. This is done by separating all the light-sources slightly in time so that they don't overlap while keeping them within the same period and thus fitting all of them within the time window

defined by the TAC. This makes it possible to utilise the instrument for spectroscopic purposes. For example, in tissue, the major constituents are water, lipids, oxy- and deoxy-hemoglobin. By using lasers at wavelengths corresponding to the absorption peaks of these four constituents and evaluating the absorption coefficients, it is obvious from Eqn. 2.5 that it is possible to estimate the concentration of each compound. The absorption coefficients of the four major absorbers in tissue and the wavelengths of the four lasers used in the TRS instruments is illustrated in Figure 3.3.

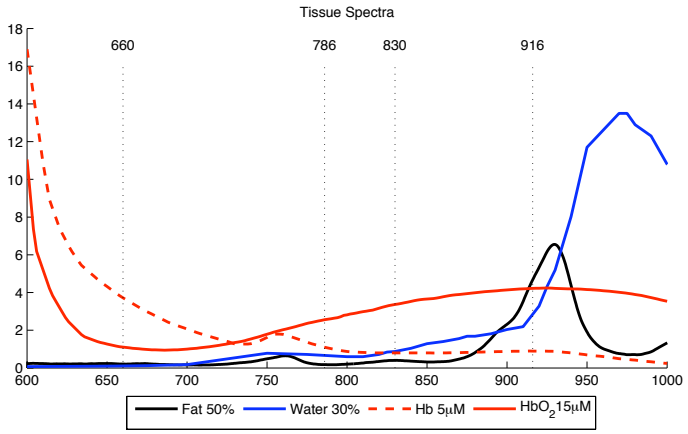

Figure 3.3: The absorption coefficients of pure Water and Fat as well as Deoxy- and Oxy-Hemoglobin at typical concentrations. Extinction coefficients taken from the literature.[18–20]

Chapter 4

White Monte Carlo

In the mid 1990's when personal computers started getting fast enough, scientists started looking at Monte Carlo as a feasible way of solving the RTE. The thoughts of using Monte Carlo to evaluate data also emerged. The advantages of Monte Carlo based data evaluation are evident as Monte Carlo is a physically more detailed model (comp. Figure 2.1). The major obstacle was the computation time as each Monte Carlo simulation can take anything from minutes to several weeks depending on the required statistical accuracy. This rendered the Monte Carlo approach useless for iterative algorithms. Graaff *et al.* presented the first ideas towards a fully scaleable model[21] partially solving the computation time problem. Scalability implies that the obtained photon distribution can be scaled with respect to some of the input parameters of the Monte Carlo simulation. Two groups simultaneously and independently presented an extension to the theory presented by Graaff *et al.*. Kienle and Patterson suggested a scalable Monte Carlo (WMC*) model[24] based on an absorptionless simulation while Pifferi *et al.* also suggested a similar technique and a method based on interpolating results from a database of Monte Carlo simulation results to be able to handle arbitrary geometries.[25] Pifferi *et al.* also showed the usefulness of the database method when evaluating actual experimental data.[26] Swartling *et al.* showed the usefulness of the WMC approach in fluorescence emission spectra modelling.[22] Swartling also raised an important question regarding the equivalency of WMC vs. traditional Monte Carlo.[3] While no group so far have shown evaluation of actual experimental data using WMC, Xu *et al.* demonstrated the superiority of the Monte Carlo based evaluation approach when comparing light propagation models for evaluation of frequency domain data, generated by a traditional Monte Carlo program.[23] Xu *et al.* also demonstrated scaling of simulations performed in absorbing media.

The idea behind WMC is to run a time resolved Monte Carlo simulation in a

*Graaf *et al.* suggested the name Condensed Monte Carlo while Kienle and Patterson called their method Mono Monte Carlo. Pifferi *et al.* picked the name White Monte Carlo as the Monte Carlo simulations were absorptionless, i.e. white. Swartling also adopted the name White Monte Carlo.[22] Xu *et al.* chose to call the method Single Monte Carlo.[23] In this work, the scaleable Monte Carlo method will be denoted White Monte Carlo (WMC).

non-absorbing medium, i.e. $\mu_a = 0$. In case of an homogenously scattering medium, the absorption for each packet is easily added post-simulation using Beer-Lamberts law:

$$w(t) = \exp(-\mu_a c' t). \tag{4.1}$$

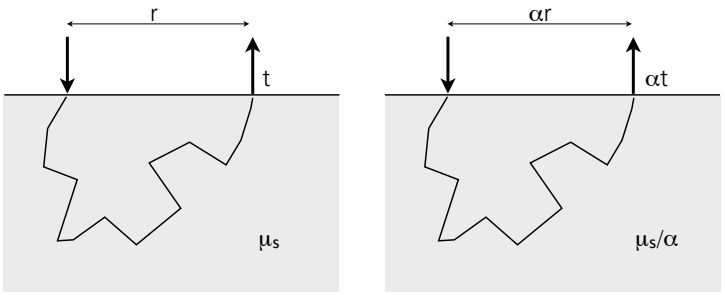

Figure 4.1: An illustration of the scaleability in mu_s in an absorption-less medium. In the simulation to the left a photon packet is propagating through a material with scattering coefficient μ_s. A a certain time t it leaves the medium at a distance r from the source. To the right is another photon packet propagating through a medium featuring a μ_s/α scattering coefficient. Assuming the same sequence of random numbers is used to calculate step-sizes and deflection angle, the packet will leave the medium at a distance αr at time αt. Adapted from Ref. 26

The scaleability in the scattering coefficient is illustrated in Figure 4.1. The idea is that μ_s only changes the step-size, Δs, while all the directional information is expressed by the anisotropy coefficient, g, and the geometry i.e. spatial variations in μ_s. If the medium is considered homogenous, linear scaling can be used for both infinite and semi-infinite geometries. However, since most Monte Carlo programs utilise some kind of spatial and temporal binning to detect photons this induces a problem as the detection grid will scale as well. This so called scaling effect,[23] reported by Xu *et al.*, arises when the sought after scattering coefficient differs a lot from the scattering coefficient used during the simulation.

4.1 Simulation Program

To utilise the WMC ideas for experimental time resolved data evaluation, a simulation program and a set of post simulation scripts were developed. Despite MCML being available as easy-to-modify open source ANSI C code, the simulation program was written from scratch with just a few snippets of code borrowed from MCML. The major reason for this is the relatively old technology used by MCML and the lack of precise numerical considerations in the existing code. The new program was written in standard C and compiled using gcc 4.0.1 for the apple darwin environment. The computer used for simulations was an Apple iMac sporting an Intel Core 2 Duo 2.16 GHz processor running OS X 10.4.10.

4.1.1 Overview

The objective was to develop a fast and accurate program to run an absorptionless Monte Carlo simulation in either an infinite or semi-infinite homogenous medium. As the intended use for the model is a forward solver (comp. Section 3.3) for the time resolved instrumentation used by the Lund group for prostate measurements, the simulation and post simulation program had a few desired properties:

- The model should be fully scaleable in μ_s' and μ_a over a large parameter space and be valid in a sufficient time interval regardless of scaling.
- As many decisions as possible should be avoided during the simulation stage, leaving them for the post simulation processing. Besides the absorption and scattering coefficients these decisions include fibre separation, temporal-binning.
- The model should be able to account for the finite spatial size of the fibres.
- The model should not impose unreasonable restrictions to the measurement geometry.
- The model should be fast enough to be feasible to use in a forward solver.

A majority of these objectives were fulfilled by using a novel detection scheme, not based on the traditional fluence-through-volume-element method but the uni-directional flow of photon packets through a mathematical plane. By launching all photon packets form the origo of a carthesian coordinate system and detecting them individually as they pass through the mathematical plane, all unwanted geometrical features were removed, eliminating the scaling problem but making post-simulation processing slightly more complicated. This photon detection scheme is illustrated in Figure 4.2.

A flowchart of the entire WMC model can be seen in figure 4.3.

4.1.2 Random Number Generation

The heart of any simulation based on sampling random number is the random number generator. The method of acquiring random numbers will affect the simulation speed as well as the accuracy of the results. As true random numbers are hard to acquire, especially in the quantities and at the speed required by modern computer simulation setups, the preferred way of generation random numbers for simulations today is to have a computer generate pseudo-random numbers by the means of mathematical algorithms. While the field of research connected with random number generation is far beyond the scope of this thesis a few things are worth mentioning. Any good pseudo random number generator should have the following properties: long period, documented which interval random numbers are generated, documented equidistribution properties in the specified interval, generate high precision random numbers, have a

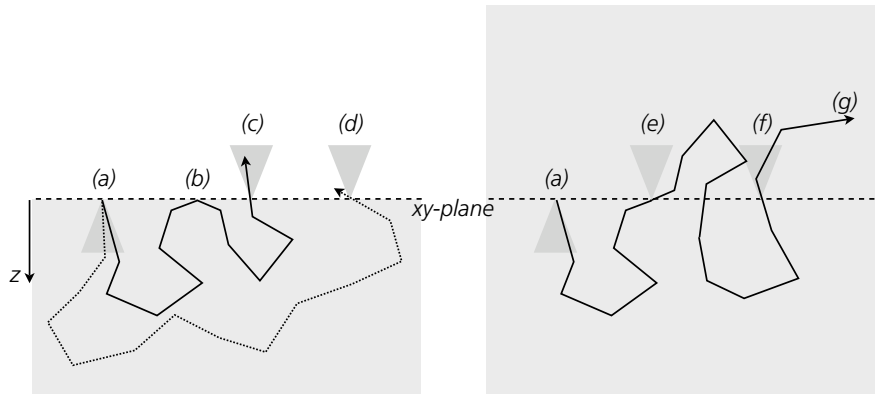

Figure 4.2: An illustration of the simulation and detection geometry in both the semi-infinite (left) and the infinite (right) case. Despite this being a rotational symmetrical problem a carthesian coordinate system is used for ease of calculations. The xy-plane is used as the detection plane so that the z coordinate can be used as a measure of depth in the semi-infinite case or simply the distance to the detection plane in both cases. (a) In both geometries the photon packets are launched from origo in a positive z-direction within the acceptance cone of the source fibre. (b) Whenever a packet have a direction and step size that would cause it to leave the medium fresnel reflection is taken into account. In this case the packet was reflected and the simulation goes on. (c) Here the packet leave the medium with an angle smaller than the acceptance cone of the detector fibre. As the detector fibre is not in place during the simulation all the packets leaving the medium are recorded without spatial restrictions. Whenever a photon packet is detected, the distance between the detection event and origo, $r = \sqrt{x^2 + y^2}$, and the total time of flight, t, is stored. As the packet leaves the medium it is terminated. (d) A packet leaves the medium outside of the acceptance cone. This means termination but no detection. (e) A photon packet crosses the detection plane with an angle outside the acceptance cone. Nothing happens and the simulation carries on uninterrupted. (f) A photon packet crosses the detection plane within the acceptance cone. The detection event-origo distance, r and total time of flight, t, is recorded. However the packet is not terminated and the simulation continuos. (g) The photon keeps propagating until it is terminated. Each photon packet can hence be detected several times. Photon packets are terminated as their total time of flight exceeds a predefined maximum, t_{max}.

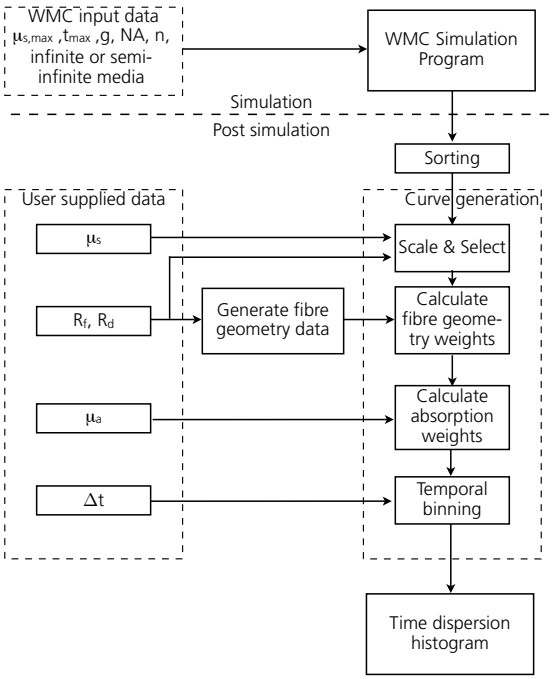

Figure 4.3: A flowchart of the forward WMC model. The input data is fed into the WMC simulation program which performs a single Monte Carlo simulation. The input parameters are, the number of photons packets to simulate, the numerical aperture (NA) of the source and detector fibres, the g-factor and two parameter, $\mu_{s,max}$ and t_{max}. t_{max} is the maximum time of flight before the photon packets are terminated in the simulation and $\mu_{s,max}$ is the scattering coefficient used in the simulation and hence the maximum scattering coefficient where the post simulation will be valid in the temporal interval $[0, \alpha t_{max}]$. The data from the simulation is sorted and used as input for a curve generation script. This script takes parameters from the user and calculates the wanted time dispersion curves. The user supplied data is the scattering and absorption coefficients, μ_s and μ_a, the source-detector fibre separation, R_d and the fibre radii, R_f, and the temporal resolution of the generated curve, Δt. The curve generation script is equivalent to the forward model box in figure 3.2

proper seeding mechanism and preferably it should be fast. Unfortunately the pseudo random number generator used by the MCML code has none of these features. The random number generation code used by MCML is taken from the book "Numerical Recipes in C: The art of Scientific Computing" by Press *et al.*, reference 27, where several different generators are presented. The one used by MCML, `ran3`, does not have a clearly stated period, and does not have state in which interval (open, closed or half open) the numbers are generated. In fact the authors of the book does not recommend the use of this generator since *"the subtractive method* [of `ran3`] *is not so well studied, and not a standard."*.[27] This is confirmed by code snippets in the MCML source code where the numbers generated are checked for out-of-interval numbers. Also, stated in the MCML source is a problem with the seeding routine. The seed, acquired from the `time()` function in C which returns the number of seconds elapsed since January 1 1970, is bit shifted from a 32 bit integer, to a 16 bit integer.

Having a 16 bit seed based on time means that the seeding will repeat itself roughly every 45 days. Yet another problem is the fact that `ran3` generate 32-bit floating point numbers, meaning 23 bit precision, while MCML converts this `float` into 64-bit (53 bit normalised mantissa, 52 actual bits) double precision floating point numbers and threats them as such.

Instead of using the old random number generator used by MCML, a state of the art generator called the Mersenne twister[28] (MT) is used in the new WMC program. More precisely the Double precision SIMD-oriented Fast Mersenne Twister[29,30] (dSFMT) version 1.1 (2007/3/22), freely available from the inventors homepage.[31] The MT is a very fast algorithm for generating pseudo random numbes, developed for Monte Carlo simulation applications. It featuring a massive $2^{132049} - 1$ period, documented superb equidistribution properties and the ability to generate double precision pseudo random number in the intervals: (0,1), [0,1) and (0,1] using all the 52 bits of precision allowed by the IEEE 754 standard.

The entire 32 bit output of the `time()` function in C is used to seed the generator which ensures unique seeds for several thousands of years as long as two simulations are not started in the exact same second.

4.1.3 Photon Launch

The photon packets are launched from origo, representing an infinitely small source, by setting their initial coordinates to $(x, y, z) = (0, 0, 0)$. Instead of using the traditional pencil beam, i.e. $(dx, dy, dz) = (0, 0, 1)$, the numerical aperture (NA) of the source fibre is taken into account. First calculating the maximum deflection angle:

$$\theta_{max} = \sin^{-1} \frac{n}{NA}, \tag{4.2}$$

where n is the refractive index of the medium, and multiplying by a random number, $\xi \in [0, 1)$, yields the deflection angle, $\theta \in [0, \theta_{max})$.

Though unnecessary in a rotational symmetric geometry, the azimuthal angle, $\phi \in [0, 2\pi)$, is generated by multiplying a random number, $\xi \in [0, 1)$, by 2π. The set of spherical coordinates, θ, ϕ, are easily transformed into Cartesian coordinates:

$$\begin{aligned} dx &= \sin\theta\cos\phi \\ dy &= \sin\theta\sin\phi \\ dz &= \cos\theta \end{aligned} \tag{4.3}$$

By taking the NA of the fibres into account, the generated simulation database is locked to fibres of a specific NA. However scaleability in the fibre diameter is still possible as all the packets are launched from the same (mathematical) point. This is conveyed in Section 4.2.2 and 4.2.2, as well as Appendix A.

4.1.4 Photon Detection

Photon detection, being a crucial part of the Monte Carlo model, were performed using a novel approach. The detection of the uni-directional fluence of photon packets through a plane has previously been used exclusively for semi-infinite and slab geometries as both feature infinite plane-like borders. The simplicity of this approach provided a foundation upon which an equivalent for infinite geometry was built. This enabled individual detection of photon packets, providing the ability to overcome the scaling effect problem encountered by Xu *et al.*,[23] by pushing the decisions on temporal and spatial binning to the post simulation side of the model.

A concern is raised regarding the detection method as a single photon packet can be detected multiple times. The question is wether the detection events can be considered independent, i.e. the probability of a photon packet being detected several times in a very small area is very low, or if the detection events have to be linked to the corresponding photon packet so that "future" detection event's can be eliminated during post processing so that a single photon packet is ensured to only be detected once. This issue is addressed during the verification, see section 5.2.

Geometrical considerations

The considered fibre geometry for the time resolved measurement to be evaluated where chosen to be two bare end optical fibres placed at the same depth (in the interstitial case) or at the surface (in the semi infinite case), with the plane ends of the two fibres in the same plane. This is of course a restriction to the possible measurement geometries but a feasible one. In theory any plane that includes origo could be used and the photons could be sent into the medium at any angle but placing the fibres in parallel means that the cylindrical symmetry can be used. This translates into a simple Monte Carlo model, where photon packets are sent into the medium at the origo, as illustrated in Figure 4.2.

Taking the into account that bare end fibres does not accept photons incident from all angles, only the photon packets passing upwards (from $z > 0$ to $z < 0$) through this plane are eligible for detection. To give the photon packets further restrictions they have to pass the detection plane within the angle of acceptance defined by the numerical aperture of the detection fibre (comp. Figure 4.2). As *a priori* information on the NA of the detector fibre is needed for this calculation, this imposes a restriction to the generated database as it is locked to fibres of a specific NA. This is ,however, the same restriction that was made for the photon launch and does thus not limit the model any further.

By restricting the detected photons to those passing through the plane in a certain direction through a narrow acceptance cone, the risk of a single photon packet producing two detection event close to each other is greatly reduced. Comparing this to traditional detection geometries, based on volumetric detection elements, such a restriction is not possible and individual packets will induce a larger, double-detection error.

Numerical considerations

The major numerical advantage of utilising the detection plane is that the entire photon paths does not have to be stored even as the photon packets are detected individually. Photon packets at all distances from the source have to be recorded due to the post simulation scaling and placing of detection fibre. A great number of detection events has thus to be recorded to provide sufficient signal to noise ratio at all fibre separations regardless of the scaling coefficient.

To reduce the amount of data from the simulation, without reducing the accuracy, the rotational symmetry of the problem was used. The symmetry axis is simply the z-axis yielding the only spatial information of interest for each recorded packet to be the source-detection event separation, $r = \sqrt{x^2 + y^2}$. Together with the temporal information, the total time of flight until the detection event, t, these are the only variables of interest for each event. Storing both of them as 32 bit floating point variables yields 64 bits of data for each detection event. This means that 2^{17} detection events can be stored per Megabyte (2^{20} bytes) of available memory of the computer running the curve generation script. Using memory efficient algorithms all the way to the temporal dispersion curve generation this means that even a database of 10^8 photon detection events can be dealt with by a computer of just 1 GB of physical memory. Comparing this to a Monte Carlo method based on traditional binning clearly illustrates the scaling effect. If scaleability is sough after in the interval $0.5 \leq \mu_s \leq 50$ [1/cm] with a temporal and spatial resolution of $\Delta t = 1$ ps and $\Delta r = 0.1$ mm respectively, over the entire scaling range. With a minimum temporal interval of validity, $t = [0, 2]$ ns and spatial validity in the range $r = [0, 30]$ mm over the entire range this would require approximately 22 GB of memory and the WMC model would still be better in the terms of spatial and temporal resolution. However, the size of the WMC-based database model will grow as more photon packets are simulated whereas the database of the Monte Carlo method utilising the traditional detection grid would have a constant size. There must hence be a S/N vs. Memory usage sweet-spot that might be worth considering in a few years time.

4.1.5 Photon Propagation

The photon propagation is very similar to any other time resolved Monte Carlo program. Each step the length of the current step is calculated using the scattering coefficient instead of the total attenuation coefficient:

$$\Delta s = \frac{-\ln(\xi)}{\mu_{s,max}}. \tag{4.4}$$

The random variable ξ is sampled in the interval (0,1], meaning Δs will be in the interval [0,∞). Since a zero step size has no meaning in a model where absorption is added post simulation using Beer-Lamberts law ξ could be sampled in the open interval (0,1) instead, meaning $\Delta s \in (0, \infty)$.

After each step the photon packet direction is changed. This is done by calculating the deflection and azimuthal angles from the current direction using

the Henyey-Greenstein function. MCML provides an excellent implementation of these calculations and this code was hence used with minor modifications to utilize the improved random number generator. When calculating the deflection angle, θ, the calculations calls for a random variable, $\xi \in [0, 1]$. As the dSFMT implementation used does not provide random variables sampled in a closed interval a semi open interval, (0,1] was used instead. As $\xi = 0$ would represent complete back scattering (comp. Eqn. 2.15) and most tissues are forward scattering ($g \approx 0.9$) using this interval will minimize the numerical error.

Apart from scattering, photon packet propagation in a nonabsorbing homogeneously scattering medium is fairly event less. The only thing that has to be checked each step taken by the photon packet is wether it crosses the xy-plane or not. In the case of an infinite medium the propagation will continue uninterrupted but in the case of a semi infinite medium fresnel reflection has to be accounted for.

An implementational difference between traditional Monte Carlo and WMC is that the WMC model is unable to handle partial reflections, i.e. depositing weight based on the reflection coefficient, as the weight of the photon packet is not kept track of. Hence when the photon reaches the border it is either reflected or transmitted. This also implies that in the semi-infinite case, the double detection problem is non-existent.

4.1.6 Photon termination

As the program was developed for evaluation of time resolved data and thus only cares about the photon distributions in a user specified time interval, $t \leq t_{max}$, energy conservation is not of importance. The photons can hence be allowed to propagate until the total time of flight exceeds that of the specified maximum time of flight, $t > t_{max}$. After that the photon packets are simply terminated.

In the semi-infinite case, photons leaving the medium are also terminated.

However, tracking photons in a highly scattering medium for long times can prove costly in the terms of computing time. Since only photon packets crossing the xy-plane are of interest, photons with zero chance of reaching the plane within the maximum allowed time can also be terminated. This condition can be expressed as:

$$(t_{max} - t) > \frac{|z|}{c'}. \tag{4.5}$$

This test is, however, computationally costly since it has to be executed very often. Even though it wasn't used in the program, as it proved to actually slow down the simulations in the parameter space of interest for this work, it is presented here for future reference. It could for example be used in a hybrid photon termination model, where check made each round is whether $t > t_{max}/k$, where k is a constant, $k \geq 2$. If this check is true, Eqn. 4.5 can be used.

4.2 Post Simulation Processing

4.2.1 Sorting

A MATLAB script to sort the simulation data by the origo-to-detection event distance, r, was written. As this is a one-time only operation speed was not of major importance but memory usage was of utter importance, hence the selection of an in-place sorting algorithm, the Combsort11.[32] This algorithm features an $O(1)$ memory usage and a worst case $O(n \log n)$ time complexity. This means that any set of data that can be loaded in the memory of the computer can be sorted within reasonable time.

The sorted data was then stored in a MATLAB struct together with all the necessary simulation data, such as the g-factor, $\mu_{s,max}$, t_{max} and the number of photons launched into the medium..

4.2.2 Curve generation

The curve generation script (comp. Figure 4.3) is the "forward model" in the data fitting procedure (see figure 3.2) and must hence be as fast as possible. Being a forward model, the script takes several input arguments and reconstructs the simulation data, providing the temporal dispersion curve for those parameters. The two major parameters are μ_s (or $\mu_s{}'$) and μ_a but the script also needs some data on the measurement, namely the fibre separation, R_d, and fibre radius, R_f, as well as the temporal channel width, Δt.

Scaling and selecting data

First a scaling coefficient, $\alpha = \mu_{s,max}/\mu_s$ is calculated. Secondly a data set with the properties, $R_d - 2R_f \leq \alpha r \leq R_d + 2R_f$, is extracted from the original dataset. The reason for the interval is explained in Appendix A. This is done very quickly since the data is already sorted. The only processing necessary is finding the two interval borders, which is very fast using a standard binary search algorithm.

The extracted t and r components are multiplied by the scaling coefficient, $r' = \alpha r$, $t' = \alpha t$.

Weighting

Each packet is assigned a weight, w_{tot}, based on absorption, $w_{abs}(t')$, through means of Beer-Lamberts law (Eqn. 4.1) and due to the fibre geometry, $w_{fibre}(r')$. The fibre geometry weight is a result of the finite size of the source and detector fibres and the integration over all angles to improve statistics, made possible by the rotational symmetry. The calculations of this weight can be seen in Appendix A. Since the fibre geometry does not change during the data fitting

procedure, all the fibre geometry data can be pre-calculated to avoid multiple calculations of the same problem.

The final weight is the product of the two weights, $w_{tot} = w_{abs}w_{fibre}$.

Binning

Temporal binning is an easy but computationally heavy task. A modified version of Shai Bagon's[33] weighted histogram MEX implementation, `whist` ,was used for speed. A weighted histogram is very similar to an ordinary histogram, but each entry is assigned a weight instead of all entries having the same weight. This means that a channel c_n will be the sum of the all the weights where $n\Delta t \leq t' < (n+1)\Delta t$:

$$c_n = \sum_{n\Delta t \leq t_i' < (n+1)\Delta t} w_{tot}(r_i', t_i'). \tag{4.6}$$

4.3 Data fitting

As discussed in Section 3.3 any forward model can be used in the iterative forward solver and utilising the WMC approach should hence be a simple case of implementing in the already existing Marquardt-Levenberg based solvers used to evaluate data using diffusion theory. However, as the WMC model is based on statistics, rather than analytical derivation, the time-dispersion histograms will have some noise in them, making the convergence of ML unsure. The effect of the noise is illustrated in Figure 4.4, where data at large source-detector separation (26 mm) in a low-scattering, high absorption phantom has been evaluated. The figure illustrates the merit function χ^2 as a function of μ_s' and μ_a minimised with respect to k:

$$f(\mu_s', \mu_a) = \min_k\{\chi^2(k, \mu_a, \mu_s')\} \tag{4.7}$$

Owing the banding structure illustrated in Figure 4.4, using the M-L algorithm to find the minimum of χ^2 with respect to all three parameters is not recommended. Instead the problem is reduced to the minimisation of

$$\tilde{\chi}^2(\mu_s') = \min_{k,\mu_a}\{\chi^2(k, \mu_a, \mu_s')\}. \tag{4.8}$$

To solve the global minimisation problem, $\tilde{\chi}^2(\mu_s')$ is now evaluated for several within a predefined interval with a specified resolution, $\Delta\mu_s'$. The resulting curve, which is basically the value of the merit function f along the valley of Figure 4.4, is shown in Figure 4.5, featuring the same data as Figure 4.4.

This also has a computation advantage as the temporal dispersion curve, c of a certain μ_a can be re-scaled to accurately estimate a curve, $\hat{c}$, with absorption $\hat{\mu}_a$ without the need for another curve extraction given that the other parameters (apart from k) is the same.

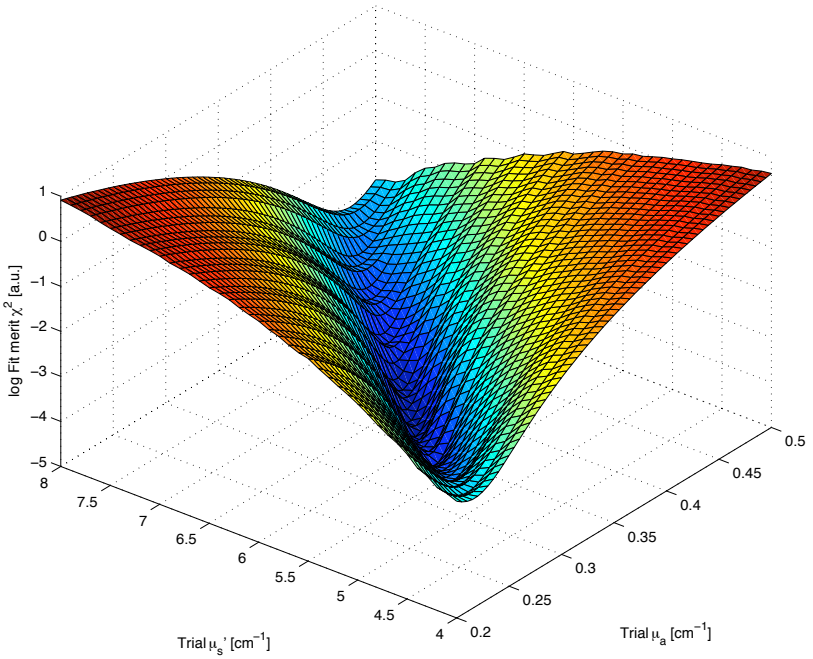

Figure 4.4: An illustration of the banding problem in an extreme case of data fitting. The bands are perpendicular to the iso-μ_a direction indicating that the bands are due to amplitude noise in the extracted curves.

For each channel, c_i, the average time, $\bar{t}_i$, is estimated or calculated during the temporal binning. The weight for that channel due to absorption is approximately:

$$w_{i,abs} \approx \exp\left(-\mu_a c' \bar{t}_i\right). \tag{4.9}$$

The estimation of $\hat{c}$ can hence be expressed using:

$$\hat{c}_i \approx c_i \exp\left(-(\hat{\mu}_a - \mu_a) c' \bar{t}_i\right). \tag{4.10}$$

This is advantageous since the curve generation is computationally heavy compared to the optimisation algorithm.

To illustrate the good fit that can be used using this method combined with the WMC method, a fit using more typical data, is illustrated in Figure 4.6.

4.4 White vs. Traditional Monte Carlo

In his Phd thesis,[3] Swartling raised the question whether White Monte Carlo is equivalent to traditional Monte Carlo as presented by Prahl *et al.*[11] Traditional

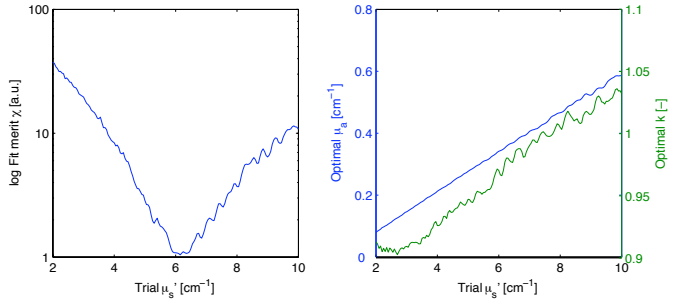

Figure 4.5: redo $\tilde{\chi}^2$!!! An illustration of $\tilde{\chi}^2$ as a function of the trial μ_s' (*left*) and the corresponding best choice of μ_a and k (*right*). The ripple from Figure 4.4 is visible, especially in the bet choice of k indicating that the ripple is due to intensity noise.

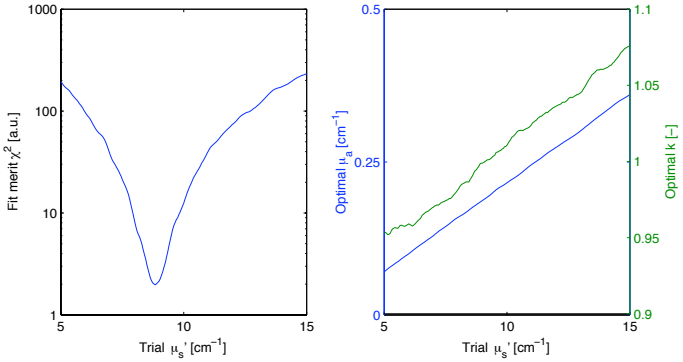

Figure 4.6: An illustration of the fit of more typical data ($\mu_s' \approx 10$, $\mu_a \approx 0.2$, 15 mm fibre separation). The smoothness of the left curve indicate that the WMC database used for fitting is sufficiently large for accurate fitting.

Monte Carlo with variable step size utilises an average $1/\mu_t$ stepsize whereas the absorption less White Monte Carlo approach uses a $1/\mu_s$ average step size. This eventually leads to different photon distributions depending on the albedo $a = \mu_s/\mu_t$ of the medium. This difference originates for the assumption in traditional Monte Carlo that the scattering dominates the absorption, i.e. $\mu_s >> \mu_a$.[13] This assumption allows quick and easy calculations of the fraction of the weight of a photon packet that should be absorbed each step: $fractionabsorbed = 1 - a$. Swartling demonstrates that this is equivalent to absorption using Beer-Lamberts law as $a \to 1$ and $a \to 0$, but notes that equivalence is not guaranteed in the intermediate region, $\mu_s \approx \mu_a$. This is, however, rather a concern for traditional Monte Carlo as the White Monte Carlo approach does not rely on the high albedo approximation, $\mu_s >> \mu_a$. Farina *et al.*[34] provide a short guide to absorption independent step size in traditional, non-white, Monte Carlo for those interested in simulating photon propagation in low-albedo media.

Chapter 5

Simulations and Measurements

5.1 Instrumentation

All the time-resolved measurements were performed using compact and portable time-domain photon migration system intended for spectroscopy of biological tissues in clinical environments.[1,35,36]

The system utilises a laser driver (SEPIA PDL 808, PicoQuant, Germany) controlling four pulsed diode lasers (LDH, PicoQuant, Germany, 660, 786, 830, 916 and 974 nm available) with wavelengths chosen to enable spectroscopy of hemoglobin, water and lipids as well as monitoring tissue oxygenation. The lasers were operated at 40 MHz at 1-2 mW output power, generating short, $<$100 ps FWHM pulses. The light from the diode lasers were coupled using short 200-μm graded index (GRIN) fibres (G 200/280 N, ART Photonics, Germany) into a single, $\sim$2 m long, 600-μm GRIN fibre (G600/840 P, ART Photonics, Germany) serving as the source fibre. A second identical fibre were used as detector fibre, guiding the light to the detector via an adjustable neutral density (ND) filter. The detector was a cooled microchannel plate photomultiplier tube (MCP-PMT; R3809-59 Hamamatsu Photonics, Japan). A TCSPC card (SPC-300, Becker&Hickl, Germany), connected to a compact PC, was used to obtain the time-dispersion histogram.

5.2 White Monte Carlo Verification

Proper verification of Monte Carlo code is important to avoid numerical glitches and to verify that the simplifications made are valid. This is usually done by comparing ones code, and/or the results, to previously published results. In the case of Monte Carlo for simulating photon transport in turbid media, results

from Van de Hulst[37] (for slab geometries) and Giovanelli[38] (for semi infinite geometries) are often used. Another popular way is to compare ones results to those provided by MCML[12] or programs derived from MCML.

5.2.1 Comparison with MCML

As no other, previously published, similar approach to Monte Carlo simulations exist and the WMC program is not based on energy conservation the validation proved a challenge as no directly comparable data was easily available. Instead MCML was modified to provide the same kind of data while making minimal changes to the original code.

Performance

The MCML code was compiled using recommended command:
`cc -o mcml mcmlio.c mcmlnr.c mcmlgo.c mcmlmain.c`
and the same line with the `-O3` optimisation level option:
`cc -o mcml mcmlio.c mcmlnr.c mcmlgo.c mcmlmain.c -O3`

The WMC code was compiled with the line:

```
gcc -msse2 -DSFMT_MEXP=132049 -DHAVE_SSE2 -O3 -fno-strict-aliasing
  --param max-inline-insns-single=1800 --param inline-unit-growth=
  500 --param large-function-growth=900 -o WMC dSFMT-src-1.1/
  dSFMT.c WMC.c,
```

as recommended by the authors of the Mersenne Twister algorithm used.

Each program were set to simulate 10000 photon packets using the following parameters:
g=0.7, n=1.33, $\mu_{s,max}$=90 cm^{-1}, t_{max}=2 ns, NA=0.29, infinite medium.

The simulation was executed 5 times for each program and the average CPU time was noted.

Accuracy

To validate the WMC simulation program code and the implementation of the scaling relationships, MCML was modified to monitor the temporal distribution of photon weight leaving a semi infinite homogenously scattering medium. Three 1 mm wide detectors, centered around 10, 15 and 20 mm recorded the time dispersion historgrams with 10 ps temporal resolution. The simulations were performed with the four combinations of $mu'_s = 5$, 10 cm^{-1}, $\mu_a = 0.1$, 0.5 cm^{-1}, with $g = 0.7$, n=1.33, 10^8 photon packets simulated.

The recorded time dispersion histograms were fitted using WMC with the following database: g=0.7, n=1.33, $\mu_{s,max}$=90 cm^{-1}, t_{max}=2 ns, NA=0.29, semi-infinite medium, , 10^9 photon packets simulated.

5.2.2 Multiple photon detection events

The perhaps biggest assumption made in the WMC program development is that of independence of the photon detection events (comp. Section 4.1.4). To study the implications of this assumption the radial distribution of the detection events of individual photon packets had to be studied. Instead of connecting the detection events to their respective photon packets, the WMC program was modified to send the photon packets, within the acceptance cone of the detector fibre, in the opposite z-direction, as illustrated in Figure 5.1. This provides an equivalent radial distribution without the need to keep track in individual photons, i.e. minimal post simulation processing. The time it takes to reach the first detection event is, however, neglected and the fraction of double-detected photons may thus be overestimated. As the risk of back scattering and hence

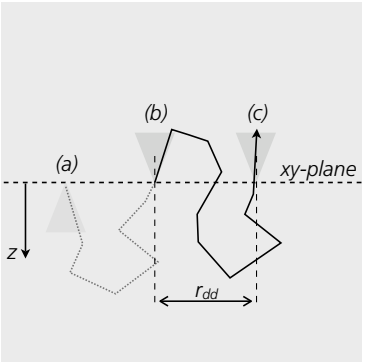

Figure 5.1: An illustration of the reversed z-direction launch WMC program. In the ordinary WMC program the photon packets would be launched at origo, (a), and later on detected at (b) and (c), the sought after distance between the two detection events, r_{dd}, would in that case have to be calculated. In the reversed program, photon packets are instead launched through the cone at (b) which is now located at origo. The detection event separation is now simply the distance from origo.

the risk of photons being back scattered back and forth over the border increases with decreasing g-factor (comp. Fig. 2.2) the simulation was performed with a fairly low g-factor to provide "worst case" data.

The parameters for the simulation using the modified WMC program where: g=0.7, n=1.33, $\mu_{s,max}$=90 cm^{-1}, t_{max}=2 ns, NA=0.29, infinite medium, 10^6 photon packets simulated.

The simulation can provide an estimate of the number of photons that contribute twice or more to the total weight of the time-dispersion histogram. Getting a more exact value is, however, difficult as the photon packets can no longer be considered as single photons with a weight according to their probability to reach the detector, but rather an infinite number of photons due to the convolution of the infinitely small source with the finite size and shape of the source fibre. Further processing of the simulation will hence not be performed in this work.

5.3 Monte Carlo vs. Diffusion

To get an estimate of the errors induced by the model and in a time-resolved measurement situation when evaluating experimental data from high absorption media using Diffusion theory two sets of simulations/evaluations were performed.

The parameter space covered was all combinations of the following parameters:

- Fibre separation, R_d: 10, 15 and 20 mm
- μ_a: 0.1, 0.25 and 0.5 cm^{-1}
- μ_s': 5, 7.5 and 10 cm^{-1}
- Fibre radius, R_f: 300 μm

5.3.1 Impulse response

The White Monte Carlo model was used to extract the impulse response temporal dispersion curves from a WMC simulation (g=0.7, n=1.33, $\mu_{s,max}$=90 cm^{-1}, t_{max}=2 ns, NA=0.29, infinite medium, $2*10^8$ photon packets simulated) for the entire parameter space defined above. The extracted curves where then evaluated using the Marquardt-Levenberg algorithm to find the parameters, $\tilde{\mu}_s'$, $\tilde{\mu}_a$ and the less interesting but important free amplitude parameter, k, corresponding to the best fit using Eqn. 2.9. The variance, σ, in Eqn. 3.1 was assumed constant. The data range used to evaluate χ^2 were 90% of maximum intensity on the rising flank to 1% of maximum intensity on the trailing flank.[39] The temporal resolution was set to Δt=10 ps.

5.3.2 With ideal IRF

The temporal dispersion curves for the parameter space were once again extracted. To mimic an actual time-resolved measurement situation the curves were also convoluted with an ideal IRF, a ∼70 [ps] FWHM gaussian pulse, illustrated in Figure 5.2. The best fit using Eqn. 2.9 convoluted with the same ideal IRF were found once again using the Marquardt-Levenberg algorithm. Once again the variance was assumed to be constant. The data range evaluated was 50% to 20% of the maximum intensity of the rising and trailing flank respectively to comply with previous data evaluation of prostate tissue.[1] The temporal resolution was set to Δt=10 ps.

5.3.3 With actual IRF

The procedure in the last section was repeated but with an actual IRF used as convolution kernel. This typical IRF is illustrated in Figure 5.3. As the

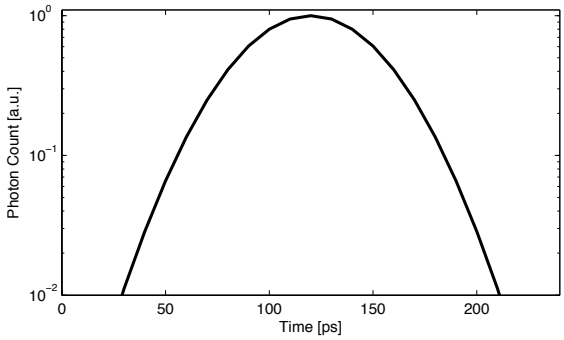

Figure 5.2: The pure gaussian IRF used as convolution kernel.

temporal resolution of the system is limited to be able to fit all four temporal dispersion curves in the time-window the temporal width of the channels were set to the typical Δt=24.43 ps.

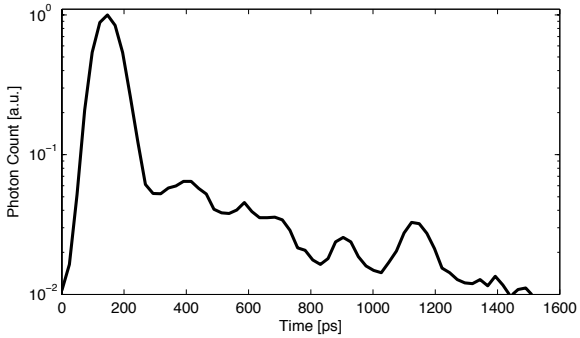

Figure 5.3: The actual IRF recorded by the system used as convolution kernel.

5.4 IRF-measurement

Evaluating old data using the WMC model it was evident that Monte Carlo alone could not solve the scattering-wavelength dependence problems reported by Svensson *et al.* Based on an paper by Schmidt *et al.*,[40] the focus was shifted to the IRF-measurement. During their IRF-measurements they introduced a thin sheet of paper just in from of the detector fibre to diffuse the incident light and *"ensure uniform excitation of all modes in the fibre bundle"*, even though GRIN-fibres supposedly have near-zero temporal mode-dispersion.

5.4.1 Arm-measurement

To observe the dispersion originating from the difference in incidence angle on the detector fibre an "arm", illustrated in Figure 5.4, was constructed.

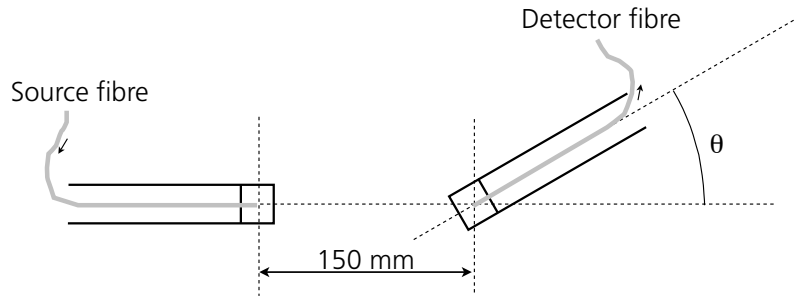

Figure 5.4: The setup for the measurements of angular dependence of the IRF measurements

The IRF's at three different angles $\theta \approx 0°$, 20°and 45°were recorded, and the experiment was repeated tree times.

5.4.2 Evaluation of real data

To study the effect on the IRF on actual data, two new ways of measuring the IRF were developed based on the ideas by Schmidt *et al.* These two ways are illustrated in Figure 5.5 together withe the old way. These three ways of measuring the IRF will hereon be referred to as blackIRF, redIRF and oldIRF. The main idea was to measure the IRF in a way that would scatter light from all angles (from the source fibre) into all angles of the detector fibre. Ideally this would be done by an infinitely thin Lambertian single-scatter diffuser positioned to minimise the fibre separation. As no such diffuser exists and would deliver to much light to the detector for the system to handle alternative solutions were sought.

blackIRF: The flat absorption spectrum and scattering properties of ordinary printer toner[41] was used in conjunction with an ordinary paper. The paper was coated with layers of toner on both sides until sufficient light absorption was achieved. While measuring the IRF the two fibres were held in close contact with the paper, aligned with each other, providing an almost zero temporal offset (paper thickness <0.1 mm).

redIRF: Thin red papers were placed on both sides of an ND filter (2 mm Schott NG4) featuring a flat absorption spectrum in the desired wavelenght region (660-916 [nm]). Red paper was choosen over ordinary white paper as it proved to have the flattest absorption spectrum of all easily available paper tested. During IRF measurements the fibres were aligned and pressed against the red paper on each side of the filter/paper sandwich.

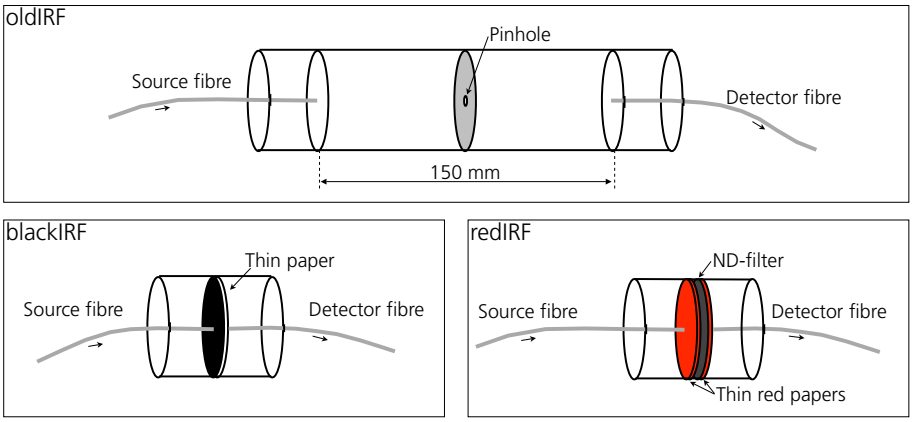

Figure 5.5: An illustration of the three ways of measuring the IRF tested. *Top:* The old way of measuring the IRF. The fibres were aligned inside a test-chamber made of black Delrin. They were separated exactly 150 mm by two stop apertures. In the middle of the chamber was a pinhole helping to minimise all reflexes. *Bottom Left:*The fibres were aligned using two black Delrin fibre-holder. A white paper coated with toner on both sides were the only thing separating the fibre ends. *Bottom Right:* Basically the same setup as blackIRF but here here an ND-filter with red paper on both sides separated the fibre ends.

To test the ways of measuring the IRF for several phantoms the test were performed in conjunction with the Absorption series further described in Section 5.5.2.

5.5 Instrument performance

5.5.1 Conditions

Phantoms

All the tissue phantoms used were based on the light scattering abilities of intralipid[42,43] and the absorption properties of India ink.[44] Pogue and Patterson provides a review of tissue simulating phantoms in Reference 45.

All phantoms were based on tap water, fresh Fresenius Kabi 200 mg/ml intralipid solution and a 1:100 stock solution of Pelikan Fount India Ink. The phantom constituents were mixed in a clear plastic container, Ø=110 mm, height 70 mm using a magnetic stirrer

Setting

The (CFD) countrates were at all times keept at ∼20 ksps.

During measurements the fibres were in place by a fibre holder featuring con-

trolls for coarse and fine height adjustments and a micrometer adjuster for the fibre separation in the range 10-30 mm. This fibre separation adjuster had a spatial offset of -0.3 mm meaning that a measurement performed at 15 mm fibre separation were actually done at 14.7 mm. For clarity the fibre separations will be denoted as integers, i.e. before the offset adjustments. However the offset was accounted for during evaluation.

WMC evaluation

All Monte Carlo evaluations were performed in the data range 50% on the rising flank to 20% on the trailing flank, using the following database unless otherwise noted:
g=0.7, n=1.33, $\mu_{s,max}$=90 cm^{-1}, t_{max}=2 ns, NA=0.29, infinite medium, $2*10^8$ photon packets simulated

5.5.2 Absorption series

An absorption series, utilising the Added Absorber technique,[46] was performed, measured and evaluated, using both diffusion and the WMC approach, using the three different IRF's.

The measurements were performed with a fibre separation of 15 mm and the fibre tips placed at a depth of 30 mm in the centre of the container. The phantom used is stated in Table 5.1: The order of measurement were: redIRF1,

Water	577 ml
Ink	(1),2,3,4,5,6,7,8 ml
Intralipid	22 ml

Table 5.1: The phantom used for the absorption series. Unfortunately the measurement of the 1 ml ink was not saved, hence the parenthesis.

blackIRF1, oldIRF1, 1 ml ink, 2 ml ink, redIRF2, blackIRF2... ending with, 8 ml ink, redIRF5, blackIRF5, oldIRF5.

5.5.3 Scattering series

A scattering series, where more and more scatterer (Intralipid) was added to the phantom in small increments using the following concentrations:
The measurements were performed with a fibre separation of 15 mm and the fibre tips placed at a depth of 30 mm in the centre of the container. The measurements were performed in rapid succession with the IRF (blackIRF) measured before and in the middle of the phantom measurements. The scattering series measurements were done outside of the temperature stabilised lab.

Water	577 ml
Ink	4 ml
Intralipid	10,12,14,...,24 ml

Table 5.2: The phantom used for the scattering series.

5.5.4 Fibre separation series

A fibre separation series was performed, using a single phantom, stated in Table 5.3, but varying the source-detector fibre separations. The fibre separations were 10-26 mm with 2 mm increments, fibre tips at 30 mm depth. The series were performed twice, with the fibre separations in ascending and descending order, with the IRF (blackIRF) measured before and after each series.

Water	577 ml
Ink	4 ml
Intralipid	22 ml

Table 5.3: The phantom used for the fibre separation series.

5.5.5 Infinite vs. Semi-infinite

In an effort to compare measurements in infinite and semi-infinite media, the phantom used in the fibre separation series (Table 5.3) was measured with the fibre tips just touching the phantom. This measurement was done at 10, 16, 20 and 26 mm fibre separation.

The semi infinite measurement were evaluated using a WMC database with the following attributes:
g=0.7, n=1.33, $\mu_{s,max}$=90 cm^{-1}, t_{max}=2 ns, NA=0.29, semi-infinite medium, 10^9 photon packets simulated

Chapter 6

Results

6.1 White Monte Carlo Verification

6.1.1 Comparison with MCML

Performance

The average CPU times for the three programs are presented in Table 6.1.1.

Program	Average CPU time [s]
WMC	13.57
MCML	21.24
MCML -O3	16.10

Table 6.1: The average CPU time of five runs simulating 10000 photon packets for the WMC and MCML (optimised/non-optimised).

Accuracy

Evaluating the time dispersion curves from the MCML simulations resulted small realtive differences between derived optical properties and MCML input parameters: -0.4±3.2% in absorption, and -1±1.4% for reduced scattering (mean±st.dev.).

6.1.2 Multiple photon detection events

The WMC simulation with reversed z-direction launch resulted in 372177 detection events. A graph showing the fraction of detection events within $2R_f$ of the reversed source is shown in Figure 6.1.

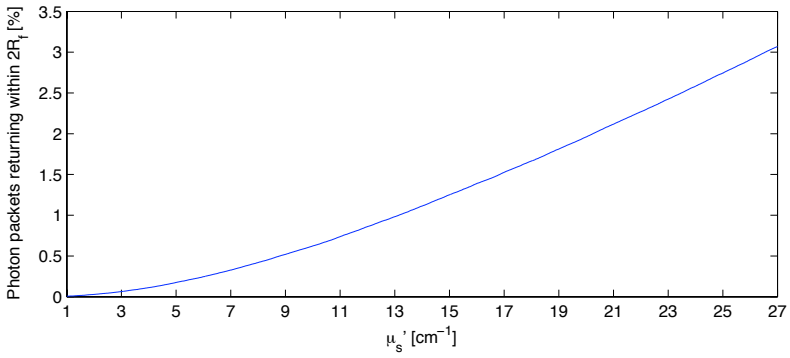

Figure 6.1: The fraction of photon packets returning within $2R_f$ from the source in the reversed WMC simulation. As the source-detection event scale with μ_s the fraction decreases as the scattering decreases.

6.2 Monte Carlo vs. Diffusion

The best fit of optical parameters, $\tilde{\mu}'_s$ and $\tilde{\mu}_a$, using diffusion theory to evaluate data from a Monte Carlo time dispersion curve of parameters μ'_s and μ_a was evaluated over a large parameter space. A summary of some data is presented in Figure 6.2 and 6.3. More data is presented in **Paper I**.

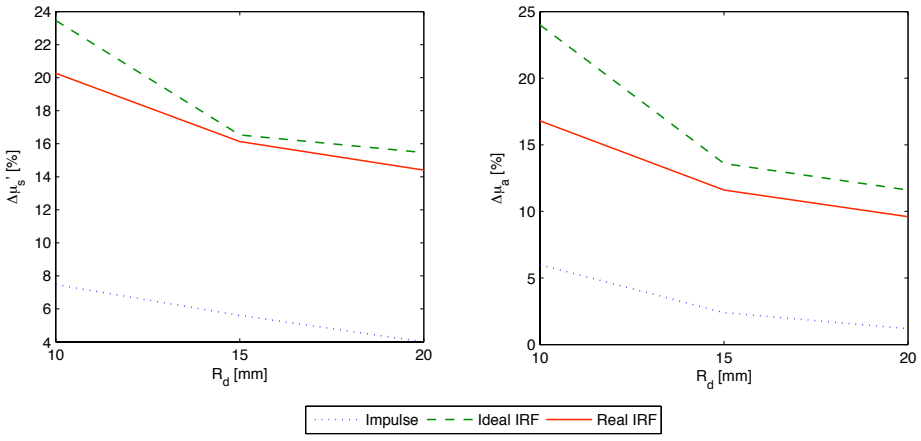

Figure 6.2: An illustration of the over-estimation of the scattering, $\Delta\mu'_s$, and the absorption, $\Delta\mu_a$, as a function of the source-detector fibre separation, R_d. The simulations used are the ones from each set (Impulse, Ideal IRF and Real IRF) with the input parameters μ'_s=7.5 cm^{-1} and μ_a= 0.25 cm^{-1}.

A few selected curves and their respective fitted Diffusion curves are presented in Figure 6.4 and 6.5.

The apprarent increase in relative error as a convolution is involved are partly due to a change in the data fitting range, which was 90% on the rising flank and 1% (90/1) for the impulse response fitting and (50/20) for the fittings involving

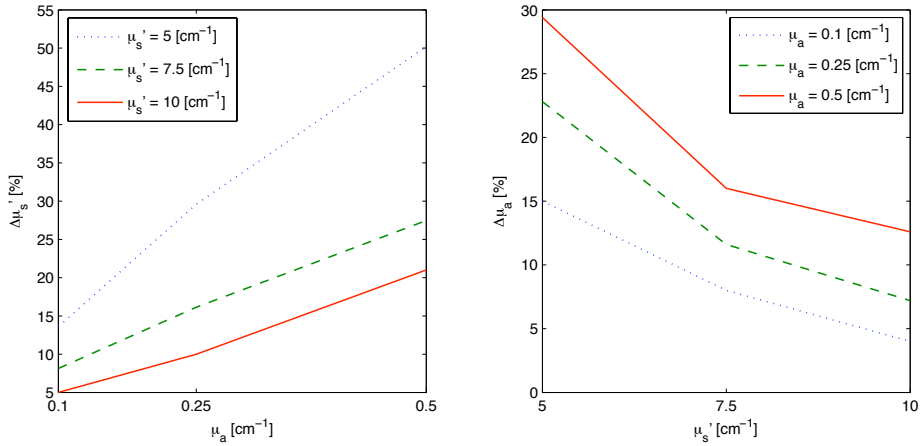

Figure 6.3: Left: The over-estimation in scattering, $\Delta\mu_s'$, as a function of the absorption, μ_a. *Right:* The over-estimation in absorption, $\Delta\mu_a$, as a function of the scattering, μ_s'. All the data is taken from the simulation involving a convolution with the actual IRF at 15 mm fibre separation.

the convolution with the IRF's. Even if a 90/1 range were to be used the effective range would be different as the convolution effectively smears out the fitting range limits as well. The 50/20 fitting range utilised is motivated by the use of this range in previously published results using the time resolved spectroscopy instrument.[1] Considering the convolution with the ideal IRF, a comparison of the 50/20 case compared to a 80/1 fitting range is presented in **Paper I** where the relative errors were found to be similar the region corresponding to prostate tissue, $\mu_a > 0.3$, $\mu_p' < 10$ cm^{-1}.

6.3 IRF-measurement

The resulting IRF's for 786 nm for the three different angles are shown normalised in Figure 6.6.

6.3.1 Arm-measurement

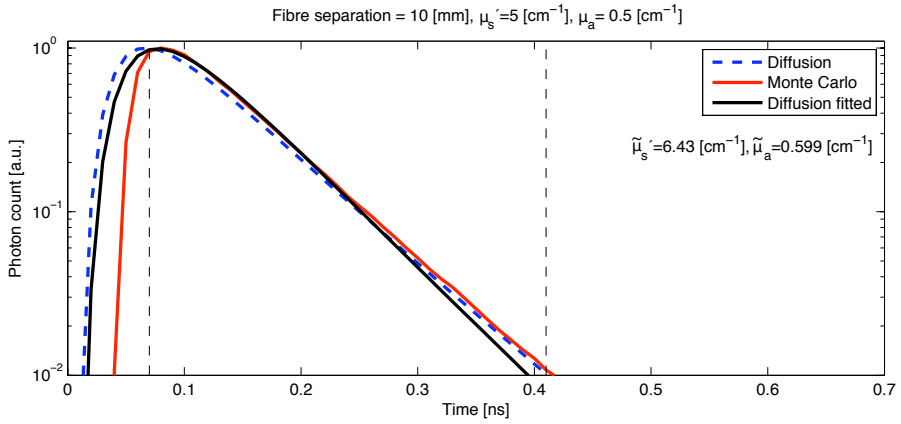

Figure 6.4: The impulse time dispersion curve for the worst case parameters. The red line shows the time dispersion curve extracted from the WMC model. The blue dashed is the curve of the same parameters from Diffusion theory and the black line is the best fit, using Diffusion theory, to the Monte Carlo curve, evaluated within the vertical dashed lines. It is evident that Diffusion theory does not model the early photons very well, causing and overestimation of both the scattering and the absorption.

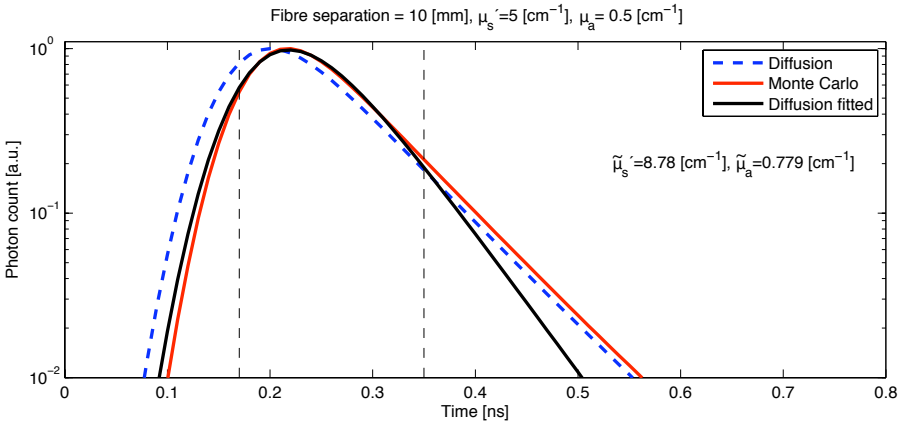

Figure 6.5: The impulse time dispersion curve for the worst case parameter, convoluted with the Ideal IRF. The red and blue dashed lines are simply their equivalents in Figure 6.4 convoluted with the Ideal IRF. The Black line is the best fit, using Diffusion theory convoluted with the ideal IRF, to the Monte Carlo curve convoluted with the ideal IRF, evaluated within the vertical dashed lines, i.e. the convolution is involved in the curve fitting procedure.

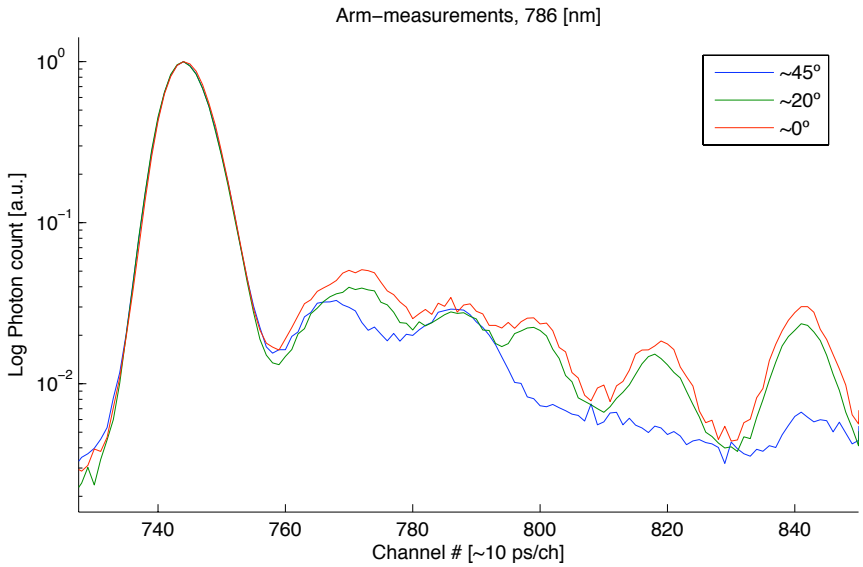

Figure 6.6: The results of the Arm-measurements for 786 nm. It is evident that there is an angular dependence as the curves 0°and 20° IRF's differ slightly. The 45° IRF is very different from the other two. It is evident that light incident at angles even far outside the acceptance cone of the fibres propagate in the fibres and reach the detector.

6.3.2 Evaluation of real data

Using Monte Carlo evaluation, the scattering in the absorption series were evaluated using the three different IRF's. The result is illustrated in Figure 6.7. For each data point, the IRF used during evaluation was the one measured closes in time to the specific data point. Comparing the IRF's as a function of time it was determined that the temporal drifts during the measurement were 1.6 ps on average over the 42 minute measurement.

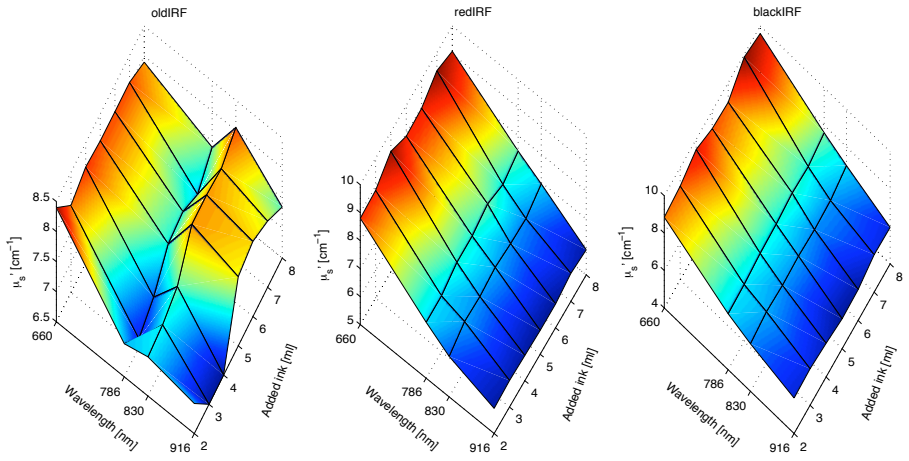

Figure 6.7: The reduced scattering as a function of wavelength and the volume of added ink, evaluated with the three different IRF's using WMC.

6.4 Instrument performance

Below is a qualitative summary of the results of the results from the experimental work. Further results, both qualitative and quantitative are presented in **Paper I**.

6.4.1 Absorption series

The measured reduced scattering and absorption as a function of the added volume of ink, evaluated using diffusion and Monte Carlo with the blackIRF are illustrated in Figure 6.8. The datasets were evaluated using the IRF measured closest in time to the dataset. The temporal drifts in the system were on average 1.6 ps over the 42 minute measurement.

6.4.2 Scattering series

The measured reduced scattering and absorption as a function of the added volume of Intralipid, evaluated using diffusion and Monte Carlo with the blackIRF

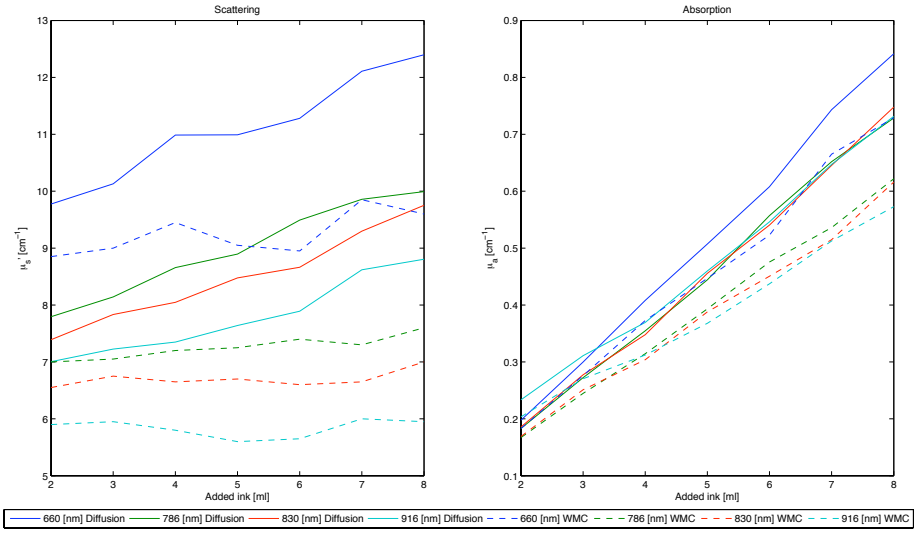

Figure 6.8: Absorption series. *Left:* The evaluated reduced scattering as a function of the volume of added ink. *Right:* The evaluated absorption as a function of the volume of added ink. *Both:* The data evaluated using Diffusion Theory is represented by solid lines and the dashed lines represent data evaluated using WMC.

are illustrated in Figure 6.9. The datasets were evaluated using the IRF measured in the middle of the dataset as the average drifts between the two IRF's was negligible and as the IRF after the measurement was not recorded as one of the fibres broke.

6.4.3 Fibre separation series

The measured reduced scattering and absorption as a function of the fibre separation, R_d, evaluated using diffusion and Monte Carlo with the blackIRF are illustrated in Figure 6.10. The second series recorded featured less temporal drift and is hence the one considered. Still the drifts were on average 2.9 ps over the 13 minute measurement. The datasets were evaluated using the IRF measured closest in time to the dataset, i.e. 26-20 mm were evaluated using the IRF taken before the measurement and 18-10 mm with the IRF taken after.

6.4.4 Infinite vs. Semi-infinite

The measured reduced scattering and absorption as a function of the fibre separation, R_d, evaluated using diffusion and Monte Carlo with the blackIRF are illustrated in Figure 6.11. The datasets were evaluated using the IRF measured closest in time to the dataset, i.e. 10 and 16 mm were evaluated using the IRF taken before the measurement and 20 and 26 mm with the IRF taken after. The average temporal drift was 1.8 ps over the 12 minute measurement.

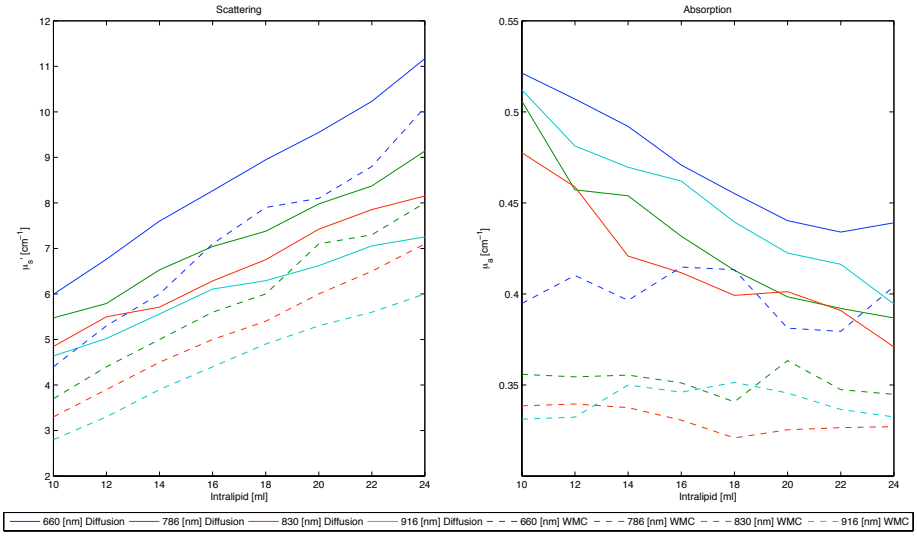

Figure 6.9: Scattering series. *Left:* The evaluated reduced scattering as a function of the volume of added intralipid. *Right:* The evaluated absorption as a function of the volume of added intralipid. *Both:* The data evaluated using Diffusion Theory is represented by solid lines and the dashed lines represent data evaluated using WMC.

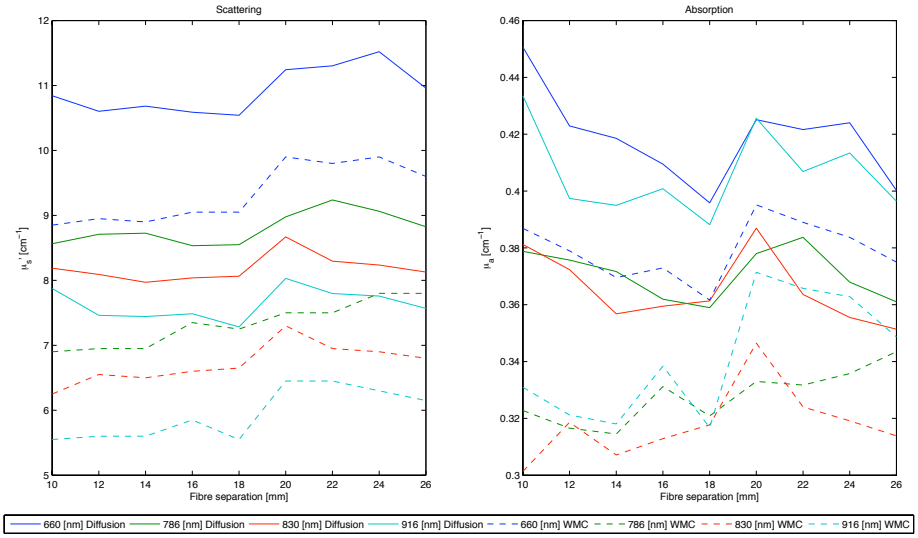

Figure 6.10: Fibre separation series. *Left:* The evaluated reduced scattering as a function of the volume of the fibre separation. *Right:* The evaluated absorption as a function of the volume of the fibre separation. *Both:* The data evaluated using Diffusion Theory is represented by solid lines and the dashed lines represent data evaluated using WMC.

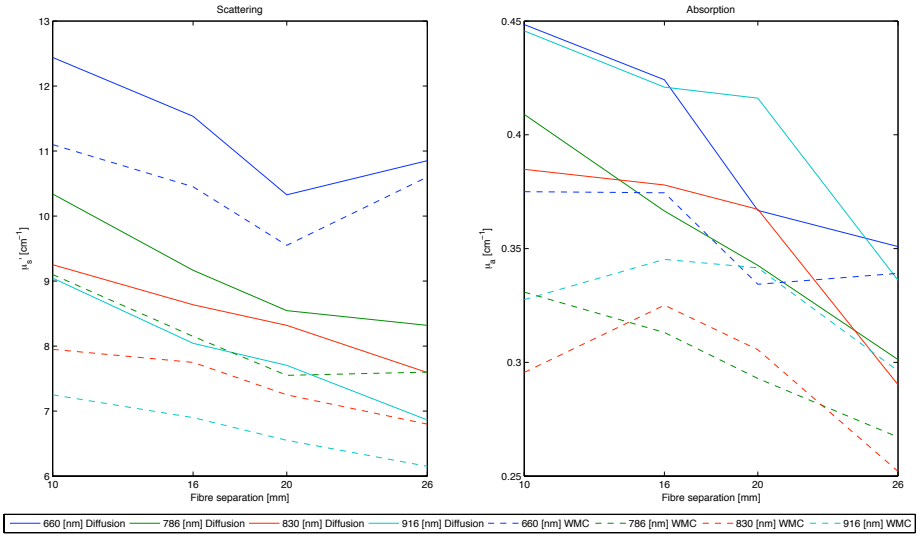

Figure 6.11: Semi-infinte geometry measurement. *Left:* The evaluated reduced scattering as a function of the volume of the fibre separation. *Right:* The evaluated absorption as a function of the volume of the fibre separation. *Both:* The data evaluated using Diffusion Theory is represented by solid lines and the dashed lines represent data evaluated using WMC.

Chapter 7

Discussion

7.1 White Monte Carlo Verification

7.1.1 Comparison with MCML

The WMC program seem to produce the similar data as the current gold standard Monte Carlo program for light transport simulations, MCML. Not surprising as the photon deflection code, being the part where a numerical mistake would be most probable, is borrowed from MCML. The deviations are actually surprisingly small considering that the WMC program used to evaluate the MCML generated time dispersion curves take fibre geometry into account. This indicate that the blunt method used in the modified MCML perhaps could be sufficient for data evaluation.

The change in pseudo number generator and the increased numerical precision does not seem to have affected the data output significantly. Detecting actual problems with the pseudo number generator used by MCML would probably require a much larger simulation and further statistical analysis. However, the new way of generating random numbers and seeding the random number generator significantly decreases the risk of repeating simulations while being the major contributor to the gain in performance over MCML. Even if the risk of repeating simulations when using MCML still is very slight, the 16 bit seed and limited period could cause problems in the future as more and more photon packets are simulated as the computers get faster and cheaper. The risk also increases if parallel or multi-core computers are used as each independent instance of the simulation require its own seed and the seed has a limited range.

In terms of simulation speed the WMC simulation program offer a slight advantage over MCML, mostly due to the highly optimised pseudo random number generator. A faster simulation program is always good news, but as the WMC databases only has to be build once perhaps it is of little importance.

7.1.2 Multiple photon detection events

The multiple photon detection problem, being the major concern during the development of the current WMC method is clearly not yet resolved. The reverse WMC program generate great data for analysis, but due to the convolution involved in the curve generation the problem turns into a surprisingly hard problem, involving integration, involving several different photon distributions, over all possible dimensions. For an accurate estimate of the actual extra weight, one also has to include a three-circle intersection calculation in these integrals, making the problem less compelling to actually solve.

However, the simulations indicate that the problem is limited and preliminary estimates indicate that the actual extra weight, i.e. the weight that is actually detected twice is well below 1%, still not counting the loss of weight due to absorption.

One can also conclude that the suggested WMC model should be better in this concern compared to any Monte Carlo model based on a volumetric detection grid, as the photon packets are only eligible for detection as they pass upwards through the detection plane and as they have to be within the relatively narrow acceptance cone of the detector fibre.

7.2 Monte Carlo vs. Diffusion

The Monte Carlo vs. Diffusion simulations considering the impulse responses confirm what has been known for a long time. The diffusion approximation is an increasingly bad approximation closer to the source and that the approximation is better at high scattering and worse at high absorption. This is mainly due to the early photons, which are not described well by Diffusion theory. This is illustrated very well in Figure 6.4 (compare the blue dashed and solid red lines) as this simulation features the worst case parameters in the simulation parameter space.

To our knowledge, no one within the field has noted or discussed the increase in the error due to the convolution with the IRF. The simulations involving the ideal IRF show that the errors are not due to the shape of the IRF from a specific instrument but applicable for all TRS instruments using a forward solver including a convolution to evaluate data. The solution is to use a better model, such as the proposed WMC model. Other solutions could be to investigate the data evaluation limits or to try out a deconvolution. This could work as the induced error most likely is due to the fact that the convolution will smear out the error of the early photons in the diffusion-based model so that the important peak cannot be included without a significant part of the early photon error being included in the evaluation.

7.3 IRF-measurement

As the WMC model did not solve the initial problems with the increasing scattering at longer wavelengths it was concluded that the problems were due to something concerning the instrumentation.

The focus was shifted towards the measurement of the IRF solely based on the article by Schmidt *et al.*[40] Comparison of the oldIRF and the way suggested there showed little difference but during data evaluation the difference was significant, regardless of the model used.

Systematic measurements to explain these differences were inconclusive. The arm measurements show some kind of angular dependance but the reason for these differences are not known. A possible solution is light traveling through the cladding of the fibres as the fibres are to short for ordinary optical fibre mode extinction to apply.

Comparing the two ways of measuring the IRF, redIRF and blackIRF little or no difference was found, indicating that the "from all angles to all angles" way of thinking is correct. A more detailed study of the influence of IRF measurements on the data evaluation could reveal not yet spotted details and could prove fruitful.

7.4 Instrument performance

7.4.1 Absorption series

The absorption series is a great example of the superiority of Monte Carlo based data evaluation compared to evaluation based on Diffusion. Neglecting the change in volume as the ink is added and assuming very low scattering of the ink[44] a constant scattering level can be assumed while the absorption should increase linearly. As predicted by simulations the scattering seem to increase as more ink is added when evaluated using the diffusion approximation but remain fairly constant when evaluated with WMC. The absorption increase linearly in both cases but as predicted by the simulations the absorption over-estimation due to the diffusion approximation model error increase as the volume of ink is increased.

7.4.2 Scattering series

The scattering series also confirms the results seen in the simulations. Neglecting the small absorption from the added Intralipid and disregarding the change in volume a constant absorption is expected while the scattering should increase linearly. The measurements show a decreasing absorption coefficient as more Intralipid is added when evaluated with Diffusion. When evauluating the same data with WMC the absorption remains roughly constrant. Scattering seem

to increase linearly in both cases but when extrapolating linearly to 0 ml of Intralipid, the diffusion-evaluated dataset exhibit large offsets, due to the model error, while WMC show much smaller offsets. Ink, featuring an approximate 0.5 albedo[44] explain a small part of this offset but further studies are required to fully understand this. One possible explanation is drifts in the system during measurements as the entire dataset was evaluated using a single IRF, due to the unfortunate fibre-breakage. As the series is performed at fairly high absorption, i.e. far from 0 ml of added Intralipid, a small drift could be the source of a relatively large offset.

7.4.3 Fibre separation series

The fibre separations series looks terrible, and the data is almost useless due to the large drifts during the measurements. The drifts were later tracked to insufficient stabilisation of the temperature in the temperature stabilised lab. A log of the temperature in the lab, a few days from the measurements is shown in Figure: 7.1

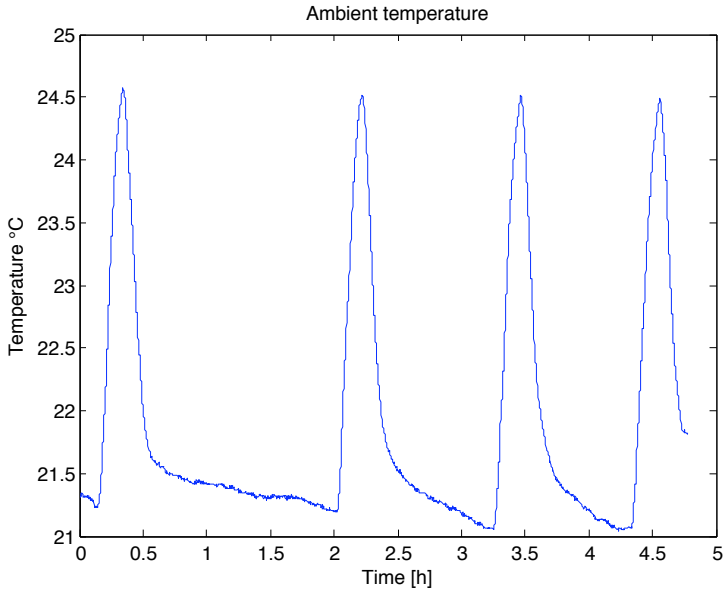

Figure 7.1: The log of the ambient temperature in the temperature stabilised lab

Even if it is unfortunate that the measurements were ruined, an important lesson can be learned from this. A temperature stabilisation system can actually negatively influence the performance of a system if the stabilised temperature is not perfectly stable. This as the stabilisation system forces the system into a non-equilibrium temperature, a small change in temperature can cause large and rapid drifts, whereas the temperature in an ordinary room is a slowly changing system. The drift will hence be slow as well and the system will have the chance

of find a new temperature equilibrium. This is a valuable lesson to learn if a new TRS system is to be built.

7.4.4 Infinite vs. Semi-infinite

Even if the semi-infinite measurements had limited drift problems the reference measurements were ruined as the fibre-separation series measurements were unusable. Another problem also occurred during these measurements. As a large portion of the light is diffusely reflected out through the border and just a small fraction of the light reaches the detector fibre end the measurements get sensitive to any reflections from objects near the phantom border. To suppress this effect all surfaces close to the phantom were covered in mate black paper. Still the reflections of the black surfaces were intense enough to be observed by the naked eye, causing a significant portion of the reflected light to re-enter the phantom. This illustrates the a problem with all semi-infinte measurements using the TSR instrument. A possible solution would be to incorporate some kind of light trap in the measurement, minimising the amount of light reflected back into the medium.

Chapter 8

Conclusions

The experimental and simulation work presented here form a strong argument that the proposed WMC method is the better photon propagation model to use when evaluating time-domain data form highly absorbing media, such as human prostate tissue. The proposed WMC model is both fast an accurate enough, regardless of the data fitting range. The proposed WMC model is valid in both infinite and semi-infinite geometries even though the semi-infinite measurements in this work were inconclusive. Evaluation of experimental data, using the WMC approach were demonstrated. A feat that has not yet been demonstrated by any other group for a fully scaleable WMC model. These results have been submitted to a peer-review journal in **Paper I**.

A new way of measuring the IRF was adapted and showed promising results. The reasons for the previous way of measuring the IRF not being good enough is still puzzling. Especially when visually comparing the new and the old IRF side by side almost no difference in the curve-shapes can be noted but apparently, during data evaluation the difference is very noticeable.

Chapter 9

Future Work

It is evident that there's much more work to be done concerning White Monte Carlo and Time-resolved spectroscopy in Lund, now that a state of the art light propagation model has been developed and the instruments seems to be working the way it's intended. The natural follow up is of course to get back in the clinic to do new measurements on prostates as this was the entire aim of this work. However, it would be a shame to leave so many questions unanswered. Below is a short list of some possible work to do:

- Construct a new IRF measurement chamber. The temporary chamber used in this work was a major obstacle when doing measurements and broke several fibres.
- Redo all measurements, especially the fibre-separation series.
- Optimise fitting procedure and make the developed software more user friendly.
- Investigate the importance of fibre geometry data.
- Investigate the effects of the model errors in the frequency domain. If the simulations indicate similar errors the developed WMC model could be of interest to a lot of people.
- Borrow the MedPhot[36] phantoms and measure them several times. This could also provide a good test for how to measure in semi-infinite geometries.
- Try measuring the series using microspheres and molecular dyes to rule out scattering effects from the ink and to understand the offsets when extrapolating the scattering series.
- Try obtaining empirical analytical expression for the time dispersion histograms provided by the WMC model to simplify the fitting procedure.
- Further study on temperature stabilisation and further work to make the system less sensitive to temperature variations.

Acknowledgements

"Research is teamwork"

This is the most valuable lesson learned over the last 6 months. With this in mind I would like to thank the entire Atomic Physics Division at Lund University for all the generous help. I would especially would like to thank Stefan Andersson-Engels for providing me this opportunity and for inviting me to the summer-school at Ven.
I am incredibly grateful for all the help provided by Tomas Svensson. Without Tomas' interest in my work and all our fun and interesting discussions this work wouldn't have gotten half way.

Thanks to the rest of the Biomedical Optics group, both present and former members, for your warm welcome and helpful support.

Thanks to Stefan Kröll and his group for sharing your labs with us.

Thanks to all my friends and family for your support and patience.

Bibliography

[1] Tomas Svensson, Stefan Andersson-Engels, Margrét Einarsdóttír, and Katarina Svanberg. In vivo optical characterization of human prostate tissue using near-infrared time-resolved spectroscopy. *Journal of Biomedical Optics*, 12(1):014022, 2007.

[2] A.J. Welch and M.J.C. van Gemert, editors. *Optical-Thermal Response of Laser-Irradiated Tissue*. Plenum Press, New York, USA, 1995.

[3] J. Swartling. *Biomedical and Atmospheric Applications of Optical Spectroscopy in Scattering Media*. Doctoral thesis, Lund Institute of Technology, Lund, 2002.

[4] M. Soto Thompson. *Photodynamic Therapy Utilizing Interstitial Light Delivery Combined with Spectroscopic Methods*. Doctoral thesis, Lund Institute of Technology, Lund, 2004.

[5] F. K. Forster. *Modellierung der Lichtausbreitung in biologischem Gewebe unter Berücksichtigung der Mikrostruktur*. PhD thesis, Fakultät für Naturwissenschaften der Universität Ulm, Germany, 2004.

[6] L. G. Henyey and J. L. Greentein. Diffuse radiation in the galaxy. *Astrophysics Journal*, 93:70–83, 1941.

[7] W. M. Star. *Diffusion theory of light transport, Optical-Thermal Response of Laser-Irradiated Tissue*, chapter 6, pages 131–206. Plenum Press, New York, USA, New York, 1995.

[8] T. Nakai, G. Nishimura, K. Yamamoto, and M. Tamura. Expression of the optical diffusion coefficient in high -absorption turbid media. *Physics in Medicine and Biology*, 42(12):2541–2549, 1997.

[9] M. S. Patterson, B. Chance, and B. C. Wilson. Time-resolved reflectance and transmittance for the noninvasive measurement of tissue optical-properties. *Applied Optics*, 28(12):2331–2336, 1989.

[10] Alwin Kienle and Michael S. Patterson. Improved solutions of the steady-state and the time-resolved diffusion equations for reflectance from a semi-infinite turbid medium. *Journal of Optical Society of America*, 14(1):246–254, 1997.

[11] S.A. Prahl, M. Keijzer, S.L. Jaques, and A.J. Welch. A monte carlo model of light propagation in tissue. *SPIE Institute Series*, IS 5, 1989.

[12] Lihong Wang, Steven L. Jaques, and Liqiong Zheng. Mcml - monte carlo modeling of light transport in multi-layered tissues. *Computer Methods and Programs in Biomedicine*, 47:131–146, 1995.

[13] Steven L. Jaques and Lihong Wang. *Monte Carlo Modeling of Light Transport in Tissues, Optical-Thermal Response of Laser-Irradiated Tissue*, chapter 4, pages 73–100. Plenum Press, New York, USA, New York, 1995.

[14] Wolfgang Becker. *Advanced Time-Correlated Single Photon Counting Techniques*. Springer Verlag Berlin Heidelberg, 2005.

[15] S. L. Jacques. Time-resolved propagation of ultra-short laser pulses within turbid tissues. *Applied Optics*, 28:2223–2229, 1989.

[16] K. Levenberg. A method for the solution of certain nonlinear problems in least squares. *Q. Appl. Math*, 2:164–168, 1944.

[17] D. Marquardt. An algorithm for least-squares estimation of nonlinear parameters. *SIAM J. Appl. Math.*, 11:431–441, 1963.

[18] Scott Prahl. Optical absorption of hemoglobin. htto://omlc.ogi.edu/spectra/hemoglobin/index.html, 2006.

[19] R. L. P. van Veen, H. J. C. M. Sterenborg, A. Pifferi, A. Torricelli, E. Chikoidze, and R. Cubeddu. Determination of visible near-ir absorption coefficients of mammalian fat using time- and spatially resolved diiffuse reflectance and transmission spectroscopy. *Journal of Biomedical Optics*, 10(5), 2005.

[20] G. M. Hale and M. R. Querry. Optical-constants of water in 200nm-200mum wavelength region. *Applied Optics*, 12(3):555–563, 1973.

[21] R. Graaff, M. H. Koelink, F. F. M. de Mul, W. G. Zijlstra, A. C. Dassel, and J. G. Aarnoudse. Condensed monte carlo simulations for the description of light transport. *Applied Optics*, 32(4):426–434, 1993.

[22] Johannes Swartling, Antonio Pifferi, Annika M. K. Enejdner, and Stefan Andersson-Engels. Accelereated monte carlo models to simulate fluorescence spectra from layered tissues. *Journal of Optical Society of America*, 20(4):714–727, April 2003.

[23] Heping Xu, Thomas J. Farrell, and Michael S. Patterson. Investigation of light propagation models to determine the optical properties of tissue from interstitial frequency domain fluence measurements. *Journal of Biomedical Optics*, 11(4):1–18, July/August 2006.

[24] Alwin Kienle and Michael S. Patterson. Determination of the optical properties of turbid media from a single monte carlo simulation. *Physics in Medicine and Biology*, 41:2221–2227, 1996.

[25] A. Pifferi, R. Berg, P. Taroni, and S. Andersson-Engels. Fitting of time-resolved reflectance curves with a monte carlo model. In R. R. Alfano and J. G. Fujimoto, editors, *Advances in optical imaging and photon migration*, volume 2, pages 311–314. Proc. Optical Society of America, 1996.

[26] Antonio Pifferi, Paola Taroni, Gianluca Valentini, and Stefan Andersson-Engels. Real-time method for fitting time-resolved reflectance and transmittance measurements with a monte carlo model. *Applied Optics*, 37(13):2774–2780, 1998.

[27] W. Press, S. Teukolsky, W. Vetterling, and B. Flannery. *Numerical Recipes in C: The art of Scientific Computing*, chapter 7.1, pages 275–286. Cambridge University Press, 2nd edition, 1992.

[28] M. Matsumoto and T. Nishimura. Mersenne twister: A 623-dimensionally equidistributed uniform pseudorandom number generator. *ACM Trans. on Modeling and Computer Simulation*, 8(1):3–30, January 1998.

[29] Mutsuo Saito and Makoto Matsumoto. Simd-oriented fast mersenne twister: a 128-bit pseudorandom number generator. In *MCQMC2006 Proceedings*, 2006.

[30] Mutsuo Mutsuo Saito. An application of finite field: Design and implementation of 128-bit instruction-based fast pseudorandom number generator. Master's thesis, Dept. of Math. Graduate School of Science, Hiroshima University, 2007.

[31] Makoto Matsumoto. Mersenne twister home page. http://www.math.sci.hiroshima-u.ac.jp/~m-mat/MT/emt.html, August 2007.

[32] Stephen Lacey and Richard Box. A fast, easy sort. *BYTE*, 16(4):315–ff., 1991.

[33] Shai Bagon. Shai bagon's matlab code, http://www.wisdom.weizmann.ac.il/ bagon/matlab.html, August 2007.

[34] B. Farina, S. Saponaro, E. Pignoli, S. Tomatis, and R. Marchesini. Monte carlo simulation of light fluence in tissue in a cylindrical diffusing fibre geometry. *Phys. Med. Biol*, 44:1–11, 1999.

[35] Tomas Svensson, Johannes Swartling, Paola Taroni, Alessandro Torricelli, Pia Lindblom, Christian Ingvar, and Stefan Andersson-Engels. Characterization of normal breast tissue heterogeneity using time-resolved near-infrared spectroscopy. *Physics in Medicine and Bololgy*, 50:2559–2571, 2005.

[36] Antonio Pifferi, Alessandro Torricelli, Andrea Bassi, Paola Taroni, Rinaldo Cubeddu, Heidrun Wabnitz, Dirk Grosenick, Michael M oller, Rainer Macdonald, Johannes Swartling, Tomas Svensson, Stefan Andersson-Engels, Robert L. P. van Veen, Henricus J. C. M. Sterenborg, Jean-Michel Tualle, Ha Lien Nghiem, Sigrid Avrillier, Maurice Whelan, and Hermann Stamm. Performance assessment of photon migration instruments: the medphot protocol. *Applied Optics*, 44(11):2104–2114, 2005.

[37] H.C. van de Hulst. *Multiple Light Scattering Vol. II.* Academic Press, New York, 1980.

[38] R. G. Giovanelli. Reflection by semi-infinite diffusers. *Optiac Acta*, 2(2):153–164, December 1955.

[39] Rinaldo Cubeddu, Antonio Pifferi, Paola Taroni, Alessandro Torricelli, and Gianluca Valentini. Experimental test of theoretical models for time-resolved reflectance. *Medical Physics*, 23(9):1625–1633, September 1996.

[40] Florian E. W. Schmidt, Martin E. Fry, Elizabeth M. C. Hillman, Jeeremy C. Hebden, and David T. Delpy. A 32-channel time-resolved instrument for medical optical tomography. *Review of scientific instruments*, 71(1):256–265, 2000.

[41] J. Swartling, J. S. Dam, and S. Andersson-Engels. Comparison of spatially and temporally resolved diffuse-reflectance measurement systems for determination of biomedical optical properties. *Applied Optics*, 42(22):4612–4620, 2003.

[42] Hugo J. van Staveren, Christian J.M. Moes, Jan van Marle, Scott A. Prahl, and Martin J.C. van Gemert. Light scattering in intralipid-10% in the wavelength range of 400-1100 nm. *Applied Optics*, 30(31):4507–4514, 1991.

[43] Stephen T. Flock, Steven L. Jacques, Brian C. Wilson, Willem M. Star, and Martin J.C. van Gemert. Optical properties of intralipid: A phantom medium for light propagation studies. *Lasers in Surgery and Medicine*, 12:510–519, 1992.

[44] Steen J. Madsen, Michael S. Patterson, and Brian C. Wilson. The use of india ink as optical absorber in tissue-simulating phantoms. *Physics in Medicine and Biology*, 37(4):985–993, 1992.

[45] Brian E. Pogue and Michael S. Patterson. Review of tissue simulation phantoms for optical spectroscopy, imaging and dosimetry. *Journal of Biomedical Optics*, 11(4):1–16, July/August 2006.

[46] B. C. Wilson, M. S. Patterson, and D. M.Burns. Effect of photosensitizer concentration in tissue on the penetration depth of photoactivating light. *Lasers in Medical Science*, 1:235–244, 1986.

[47] S. A. Prahl. *Light Transport in Tissue.* PhD thesis, University of Texas at Austin, 1988.

[48] Lihong Wang, Steven L. Jacques, and Liqiong Zheng. Conv-convolution for responses to a finite diameter photon beam incident on multi-layered tissues. *Computer Methods and Programs in Biomedicine*, 54:141–150, 1997.

[49] Eric W. Weisstein. Circle-circle intersection. From Mathworld–A Wolfram Web Resource. http://mathworld.wolfram.com/Circle-CircleIntersection.html, August 2007.

Appendix A

Fibre geometry calculations

The WMC simulation program does not in any way consider the fibre geometry, leaving it for post processing of the simulation data. This is easily done as both the source and each detection lack spatial size, i.e. they are pure mathematical points. This means that fibre size's and irradiance distributions can be emulated using a simple convolution and multiplication. The idea of convoluting output data from Monte Carlo simulations have previously been conveyed by Prahl[47] and Wang and Jacques.[48] However, their calculations differ from what have been used in this work as individual photon packets are considered.

Throughout this work it is assumed that both the source and detector fibres has the same radius, denoted R_f and that they both exhibit a uniform near field irradiance distribution/spatial response, i.e. the source fibre have a top-hat emission profile and the source fibre, transmit equal amounts of light, regardless of where on the fibre end the light is incident.

A.1 Calculations for Monte Carlo data evaluation

All the necessary notation for this section is illustrated in figure A.1. To use the circular symmetry around the source, the overlap function O is integrated over all angles, θ, removing the need to store any spatial information but R_p for each photon packet detection event. This also makes use of all photons, improving overall statistics.

Please note that the source-photon separation R_p is the same distance as the already scaled r' in section 4.2.2. The name R_p is used here for clarity as there are many radii to keep track of.

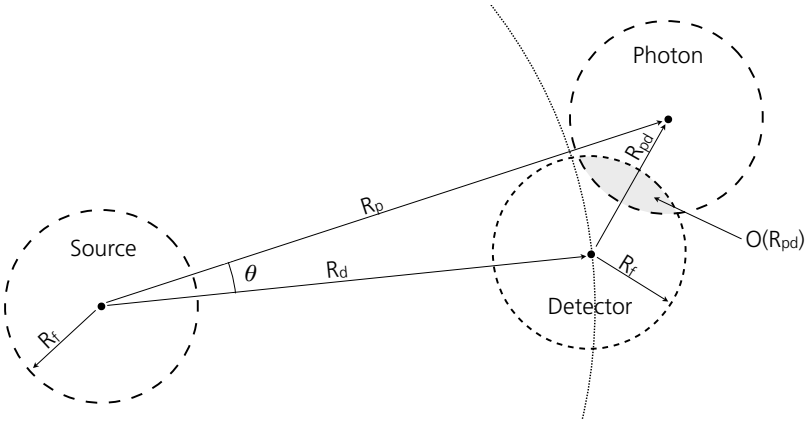

Figure A.1: An illustration of the source and a single photon packet, before convolution, as points, and after convolution with the source fibre irradiance distribution, coarse dashed circles. The source-photon distance, denoted r in the rest of this thesis is here denoted R_p. R_d is the user supplied source-detector fibre distance, also illustrated with a dotted circle, and θ is the angle between R_p and R_d. R_{pd} is the detector-photon distance and $O(R_{pd})$ is the area of overlap between the detector fibre and the photon (convoluted with the source fibre irradiance responce). R_f is the radius of both the source and detector fibre.

A.1.1 Normalised Overlap function

The normalised overlap function for two circles of the same size at distance R_{pd} from each other is:[49]

$$O(R_{pd}) = \frac{2}{{R_f}^2\pi}\left({R_f}^2 \arccos\left(\frac{R_{pd}}{2R_f}\right) - \frac{R_{pd}}{2}\sqrt{{R_f}^2 - \frac{{R_{pd}}^2}{4}}\right) \tag{A.1}$$

A.1.2 $R_{pd}(\theta)$-function

For a single photon packet detection event, i.e. R_p and R_p are fixed, R_{pd} does only depend on the angle θ and the relation can be expressed:

$$R_{pd}(\theta) = \sqrt{{R_p}^2 + {R_d}^2 - 2R_dR_p\cos(\theta)} \tag{A.2}$$

$$= \sqrt{e - f\cos(\theta)} \tag{A.3}$$

where e and f are constants.

Using the small angle approximation:

$$\cos(\theta) \approx 1 - \frac{\theta^2}{2},$$

Eqn. A.2 can be written as:

$$R_{pd}(\theta) = \sqrt{2R_pR_d}\sqrt{\left(\frac{R_p^2+R_d^2}{2R_pR_d}-1\right)+\frac{\theta^2}{2}} \quad (A.4)$$

$$= g\sqrt{h+\frac{\theta^2}{2}}, \quad (A.5)$$

where g and h are constants.

A.1.3 Evaluating integration limits

Eqn. A.1 is only valid in the $0 \leq R_{pd} \leq 2R_f$ interval. Hence the integration limits θ_0 must be found. θ_0 is the angle where the photon and detector circles tangent each other, i.e. when $R_{pd} = 2R_f$ This also explains the $R_d - 2R_f \leq R_{pd} \leq R_d + 2R_f$ data extraction limits in section 4.2.2.

$$\theta_0 = \arccos\left(\frac{{R_p}^2+{R_d}^2-(2R_f)^2}{2R_pR_d}\right). \quad (A.6)$$

A.1.4 The integration

With the above equations in mind, the weight originating from the fibre geometry is:

$$w_{fibre} = \int_0^{2\pi} O\left(R_{pd}(\theta)\right)d\theta = 2\int_0^{\theta_0} O\left(R_{pd}(\theta)\right)d\theta \quad (A.7)$$

This integral can be solved numerically but a faster way would be to find an approximate analytical solution.

Analytical solution

The first step in finding an approximate analytical solution is to approximate Eqn. A.1 with a third order polynomial:

$$O(R_{pd}) \approx a{R_{pd}}^3 + b{R_{pd}}^2 + cR_{pd} + d. \quad (A.8)$$

The coeffiecients a, b, c, and d, depend only on R_f and can be calculated numerically.

Inserting Eqn. A.3 and Eqn. A.5 where necessary into Eqn. A.8 yields:

$$2\int_0^{\theta_0} O\left(R_{pd}(\theta)\right) d\theta \approx \quad 2a\int_0^{\theta_0} g^3\left(h+\frac{\theta^2}{2}\right)^{3/2} d\theta \tag{A.9}$$

$$+ \quad 2b\int_0^{\theta_0} \left(e - f\cos(\theta)\right) d\theta \tag{A.10}$$

$$+ \quad 2c\int_0^{\theta_0} g\left(h+\frac{\theta^2}{2}\right)^{1/2} d\theta \tag{A.11}$$

$$+ \quad 2d\int_0^{\theta_0} d\theta \tag{A.12}$$

The two integrals, (eqn .A.10) and (eqn. A.12)), are easily solveable. The other two integrals require the small angle approximation to be easily solvable and are thus presented in this form.

The solutions to the four integrals are presented below:

$$\begin{aligned}
\int_0^{\theta_0}\left(h+\frac{\theta^2}{2}\right)^{3/2} d\theta &= \frac{3}{8}h^2\sqrt{2}\left(-\ln(2)-\frac{\ln(h)}{2}+\ln\left(\theta_0\sqrt{2}+\sqrt{4h+2\theta_0^2}\right)\right) \\
&\quad +\frac{1}{16}\theta_0\left(\frac{1}{2}\left(4h+2\theta_0^2\right)^{3/2}+3h\sqrt{4h+2\theta_0^2}\right) \\
\int_0^{\theta_0}\left(e-f\cos(\theta)\right) d\theta &= -\left(-e\theta_0+f\sin(\theta_0)\right) \\
\int_0^{\theta_0}\sqrt{h+\frac{\theta^2}{2}} d\theta &= \frac{1}{4}\left(\theta_0\sqrt{4h+2\theta_0^2}-h\sqrt{2}\ln(h)\right) \\
&\quad +h\frac{1}{\sqrt{2}}\left(\ln\left(\theta_0\sqrt{2}+\sqrt{4h+2\theta_0^2}\right)-\ln(2)\right) \\
\int_0^{\theta_0} d\theta &= \theta_0
\end{aligned}$$

This sums up to:

$$w_{fibre} = 2\int_0^{\theta_0} O\left(R_{pd}(\theta)\right) d\theta \approx \tag{A.13}$$

$$\begin{aligned}
- \quad & 2b\left(-e\theta_0+f\sin(\theta_0)\right)+2d\theta_0+\frac{1}{16}ag^3\theta_0\left(4h+2\theta_0^2\right)^{3/2} \\
- \quad & h\sqrt{2}\left(cg+\frac{3}{4}ag^3h\right)\left(\ln(2)+\frac{\ln(h)}{2}\right) \\
+ \quad & \left(cg+\frac{3}{4}ag^3h\right)\left(\frac{1}{2}\theta_0\sqrt{4h+2\theta_0^2}+h\sqrt{2}\ln\left(\theta_0\sqrt{2}+\sqrt{4h+2\theta_0^2}\right)\right)
\end{aligned}$$

A.1.5 Spatial binning

Even if the analytical solution is faster than a numerical integration of Eqn. A.7 the analytical expression still has to be evaluated for each photon packet, a task

that does take some time. To solve this problem, a spatial binning of the photons is suitable. This is done by dividing the interval $R_d - 2R_f \leq R_{pd} \leq R_d + 2R_f$ into several smaller interval of width ΔR,

$$R_d - 2R_f + n\Delta R \leq R_n < R_d - 2R_f + (n+1)\Delta R.$$

The weight for each interval, $w_{n,fibre}$, can be calculated outside of the curve generation script (comp. figure 4.3). Since this calculation only has to be performed once the number of intervals can be very large without any performance loss and increased accuracy. During the data weighting procedure the each photon packet is assigned the fibre geometry weight according to which interval its source-detection event distance falls into. It might seem as this makes the analytical solution presented above obsolete but for it might prove useful if, one day, the source-detector separation from a measurement with known optical properties has to be evaluated.